Precision measurement of the $2\,^3P_1$-to-$2\,^3P_0$ fine structure of atomic helium using frequency-offset separated oscillatory fields

Farshad Heydarizadmotlagh

A Thesis Submitted to the Faculty of Graduate Studies
In Partial Fulfillment of the Requirements
for the Degree of Master of Science

Graduate Program in Physics and Astronomy

York University
Toronto, Ontario

May 2025

Abstract

Increasing accuracy of the theory and experiment of the n=2 ^{3}P fine structure of helium has allowed for increasingly-precise tests of quantum electrodynamics (QED), determinations of the fine-structure constant α, and limitations on possible beyond-the-Standard-Model physics. Presented here is a 2-part-per-billion (ppb) measurement of the J=1-to-J=0 interval. The measurement is performed using the frequency-offset separated-oscillatory-fields (FOSOF) method. The result of $29\,616\,955\,018(60)$ Hz represents a landmark for helium fine-structure measurements, and, for the first time, will allow for a 1-ppb determination of the fine-structure constant when QED theory for the interval is improved.

Dedicated to Majid, my dear father and Fariba, my beloved mother.

Acknowledgements

I would like to first thank Professor Eric Hessels, my supervisor, for providing me with the opportunity to experience physics through such an exciting experiment and for sharing his wealth of knowledge and wisdom with me throughout the project. I would also like to thank my co-supervisor, Professor Matthew George, who has been a teacher, a professor, and a supervisor to me at different times throughout my academic journey, but a friend and dear mentor to me at all those times.

I would like to thank the person who taught me everything I knew about running the experiment, Taylor Skinner, through heroic effort and with an abundance of patience, which dealing with me definitely demanded at times. I would also like to thank Kosuke Kato, whose hard work laid the foundations of all we have achieved.

I would like to thank Neil McCall, the person who is the closest thing I have had to a brother. His wisdom, patience, and friendship are the only reason that I managed to maintain my sanity at some of my most challenging times. It is thanks to Neil that I ever dared to dream bigger than I had previously permitted myself, as his relentless optimism is a fuel most potent.

I would also like to thank Jorge Garcia Perez and Ushieja De Zoysa for being great friends and all the conversations and moments that we had. It was also a pleasure to get to know and work with all the great people in the EDM^3 collaboration. I will hold dear the memories I made with my friends Tom, Ryan, Sunna, Tina, Coral, Chris, Abteen, and others at and outside of York university.

I have great admiration and appreciation for the hard work done by the York University staff, especially the great people in the physics and astronomy department. I have to give special thanks to Cristal for all the times she helped me out of a bureaucratic situation I found myself in. I want to thank Professor William Pietro, whose presence and support has been a blessing that I will never forget. I have greatly enjoyed and learned from my conversations about physics with Professor Randy Lewis, who is an angel of a man universally loved by all students. I would also like to thank Professor Adam Muzzin, the current graduate program director of the physics and astronomy department, for his valuable guidance through the process of working on my thesis. I want to thank Professors van Wijngaarden, Lever, McCall, Mermut, Horbatsch, and many others who mentored and shaped me into who I am today.

It is also important for me to mention my friends and family back in Iran. I will forever cherish my memories growing up in Iran and the times we had together dearly. I also will forever remember my brilliant teachers in Sampad (my school in Iran) who invoked a sense of curiosity and wonder in me since I was a child.

And finally and most importantly, I want to thank my dear parents Majid and Fariba. I am nothing without them and it is only thanks to their innumerable sacrifices that I am here. They both uprooted a much more comfortable life in Iran and went through the herculean effort of immigration for their only child. My father Majid has been my source of strength and is my personal hero. He is a man known for his dependability and honour, which is a standard I shall always strive for. My mother Fariba has always been the light in our lives even in the darkest of moments, always managing to make our days a little brighter, never showing the pain she might have been in. Thanks mom and dad, I could not have done any of it without you.

Table of Contents:

List of Tables

List of Figures

1. Introduction

1.1. Fine-structure Constant

The fine-structure constant (α) is a dimensionless universal constant which describes the strength of electromagnetic interactions. In terms of quantum-electrodynamics (QED), α defines the strength of interaction between photon and electron fields, as it is directly related to the coupling constant between the two fields. It has a value of approximately $\frac{1}{137}$ and is described in terms of SI units as

$$\alpha = \frac{1}{4\pi\epsilon_\circ}\frac{e^2}{\hbar c},$$

where e is the elementary charge, $\hbar$ is the reduced Planck constant, c is the speed of light, and $\epsilon_\circ$ is the vacuum permittivity.

To find the fine-structure constant from the precision measurement of an atomic transition, a QED calculation of similar precision is required to describe the transition energy in terms of the fine-structure constant. As a result, a high-precision atomic transition measurement can be used either to test QED predictions or to determine α. As shown in figure 1.1, current measurements of α obtained from atomic recoil [1, 2] and the electron magnetic moment (g_e) [3] disagree by more than 1 part-per-billion (ppb). A ppb measurement of helium fine structure is valuable as it both serves as a test for QED theory and provides an additional check on the other α measurements.

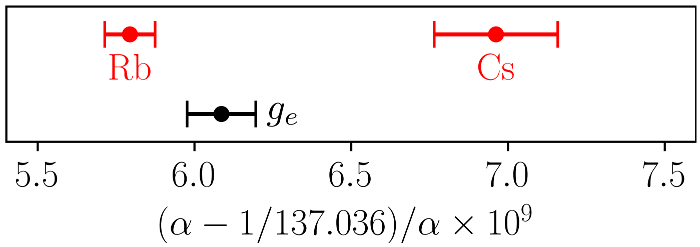

Figure 1.1: Current determinations of α obtained from atomic recoil in Rb [2] and Cs [1] and from the electron magnetic dipole moment (g_e) [3]. The determinations span a range of over 1 ppb.

1.2. Measurement of Helium Fine-Structure

In 1964 Schwartz suggested [4] that the n=2 ^{3}P states of helium could allow for a more precise determination of the fine-structure constant α than could be derived from studying the 2P fine structure of hydrogen, given that helium has a 60-times-longer lifetime and a three-times-larger interval. He suggested that a part-per-million determination of α might be possible if improvements were made in both theory and experiment. In the intervening decades, experimental measurements have shown continual improvements [5–25]. The evaluation of new systematic effects [26–30] has improved the agreement between these measurements. Quantum-electrodynamic theory [31–53] for these intervals has also advanced greatly with a complete calculation of all terms of order α^6 (times mc^2) [37] in 1972, and all terms of order α^7 being completed [51] in 2010. This improved theoretical precision and the four orders of magnitude of improved experimental precision since 1965 [54] are illustrated in figure 1.2.

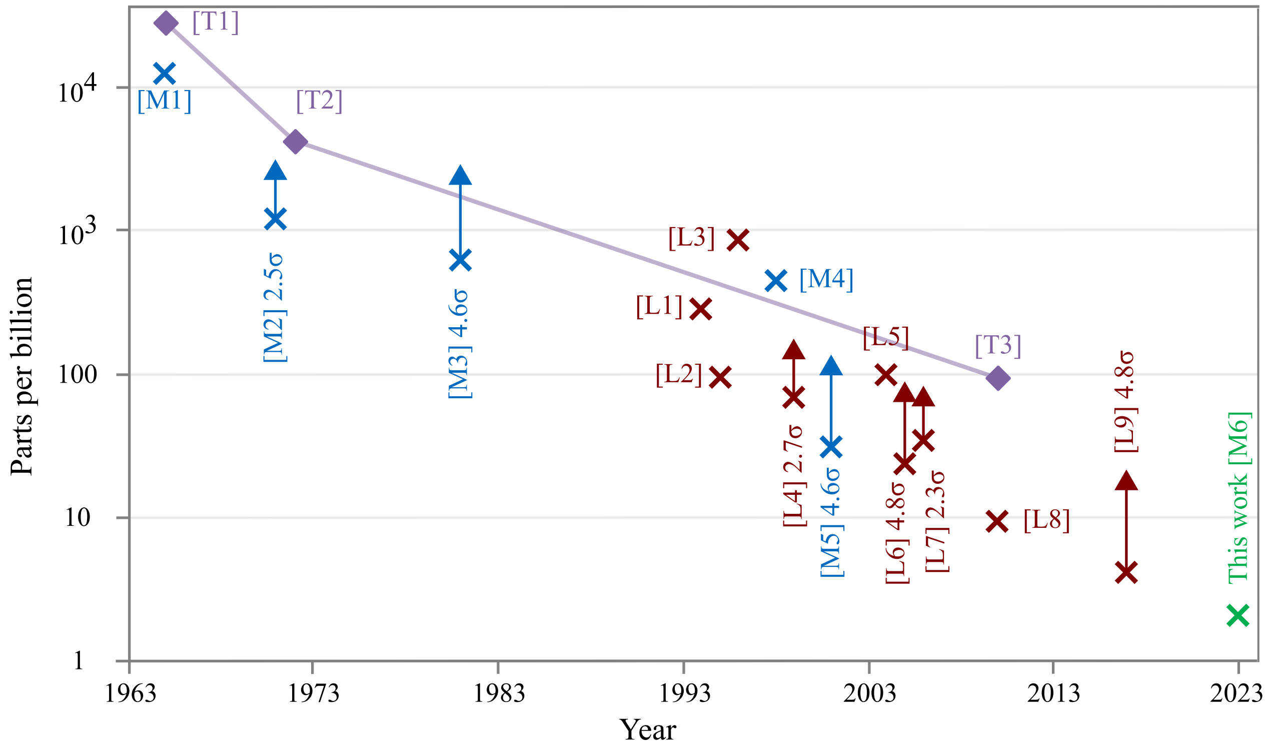

Figure 1.2: The history of improvement in precision of measurements and theory for the helium 2^3P fine structure. The exes (shown in various colours for clarity of labelling) indicate the quoted uncertainty in parts per billion (ppb) for measurements of the J=0-to-J=1 and J=0-to-J=2 intervals performed since 1965. For measurements that disagree with this work, the number of standard deviations (σ) for this disagreement is indicated, and the arrows show the expanded uncertainty that would be required for agreement. The purple diamonds show the theoretical precision, which has improved with the completion of calculations of all contributions of order α^6 (T2) and α^7 (T3). Calculations of α^8 terms will allow for a ppb-level comparison between experiment and theory. The points on the figure are categorized into three groups: theoretical calculations T1 [31], T2 [37], and T3 [51]; laser measurements L1 [9], L2 [10], L3 [13], L4 [14], L5 [15], L6 [18], L7 [17], L8 [12], and L9 [24]; and microwave measurements M1 [54], M2 [6], M3 [8], M4 [19], M5 [21], and M6 [55].

The theoretical calculation of the $2\,^3P_2$-to-$2\,^3P_0$ transition energy (ν_{20}) is much more precise than calculations of either of the two sub-intervals ($2\,^3P_2$-to-$2\,^3P_1$ (ν_{21}) and $2\,^3P_1$-to-$2\,^3P_0$ (ν_{10})), given the absence of singlet-triplet mixing effects in the combined interval [49]. Since the $2\,^3P_2$-to-$2\,^3P_0$ transition requires a two-photon process, the power required to drive it is exceedingly high. As such, to make a high-precision measurement of the full interval, it is advantageous to measure each sub-interval separately and then combine the two measurements. The combination of a complete calculation to order α^8, the current measurement, and the previous measurement by our group [25] of the $2\,^3P_2$-to-$2\,^3P_1$ interval will allow for a determination of α at a level of 1 ppb, one thousand times more accurate than the proposal of Schwartz [4].

A ppb-level comparison between experiment and QED calculations will have wide-ranging implications. It will provide the most accurate test to date of QED in a multi-electron system [56]. This comparison will allow the 2^3P fine structure to be used for a direct test for beyond-the-Standard-Model physics [56], such as exotic spin-dependent interactions between electrons [57] (at 100 times the accuracy of current tests).

The most precise determinations of α, based on the electron magnetic moment (g_e) [3, 58–61] and atomic recoil [1, 2], currently show discrepancies of more than 1 ppb, as shown on figure 1.1. Comparison of determinations of α obtained from various systems allows for tests of beyond-the-Standard-Model physics in each of the systems [3, 62–64].

2. Measurement Technique

In this chapter, a theoretical description of the technique used for this measurement is discussed.

2.1. Introduction to FOSOF

The technique used in the current measurement is the frequency-offset separated-oscillatory-fields (FOSOF) method [65], which is a modification of the Ramsey method [66] of separated oscillatory fields (SOF). FOSOF has previously been used to measure the atomic hydrogen Lamb shift [67] and the 2^3P_2-to-2^3P_1 transition in helium to ultrahigh precision [25].

The Ramsey method of separated-oscillatory-fields, also known as Ramsey interferometry, involves excitation of an atomic population by two consecutive pulses of oscillating electromagnetic waves separated in time (as shown in figure 2.1 (a)), with both tuned to drive the same atomic transition. The method results in two quantum-mechanical amplitudes for atoms to be driven into the excited state (by either of the pulses, as shown in figure 2.1 (b)). Since the pulses are time-separated, the two amplitudes accrue different quantum-mechanical phases, causing interference between them. This interference introduces features referred to as Ramsey fringes in the line-shape (as shown in figure 2.1 (c)). These fringes can have widths that are smaller than the natural line-width. The SOF line-shape for a two-level system exposed to two ideal pulses of duration D and separation T (as shown in figure 2.1(a)) is

$$P(T, D, V, \Delta\omega, \Delta\phi) = \left(\frac{DV}{\hbar}\right)^2 \cos^2\left(\frac{T\Delta\omega + \Delta\phi}{2}\right) \operatorname{sinc}^2\left(\frac{D\Delta\omega}{2}\right), \tag{2.1}$$

where $\Delta\omega$ is the angular frequency difference between the applied microwave frequency and the atomic resonant frequency ($\Delta\omega = \omega - \omega_0 = 2\pi(f - f_0)$), V is the magnetic-dipole matrix element driving the transition, and $\Delta\phi = \phi_2 - \phi_1$ is the phase difference between the microwave fields in the two pulses [68].

In the SOF method, since both pulses have the same frequency, the interference depends on the relative phase of the two pulses $\Delta\phi$, giving constructive interference on resonance when $\Delta\phi = 0$ and destructive interference when $\Delta\phi = \pi$. Figure 2.1 (c) shows the difference between SOF signals taken at these two values of $\Delta\phi$.

FOSOF is a modification of the SOF method. For the FOSOF method, a small frequency offset of $-\delta f$ is applied to the microwave frequency of the first pulse, with a frequency offset of $+\delta f$ applied to the second pulse. These offsets introduce a time-dependent component to the phase difference between the two microwave fields. In essence, FOSOF measures the interference signal not just at phase differences of $\Delta\phi = 0$ or $\Delta\phi = \pi$, but at all values of $\Delta\phi$. As a result, the FOSOF atomic signal for a fixed f and δf varies sinusoidally in time. The phase of this atomic signal minus the phase of the beat signal that is obtained by combining the two microwave fields is defined to be $\Delta\theta$, which is the quantity measured in the FOSOF technique.

For a two-level system with two ideal pulses of duration D and separation T (as in figure 2.1 (a) and (b)), the FOSOF line-shape is [68]

$$\Delta\theta(f) = (T - D)\Delta\omega + 2\arctan\left[\frac{\Delta\omega \tan\left(\sqrt{4V^2 + \Delta\omega^2}D/2\right)}{\sqrt{4V^2 + \Delta\omega^2}}\right], \tag{2.2}$$

where V is the magnetic-dipole matrix element driving the transition and $\Delta\omega/2\pi = f - f_0$ is the

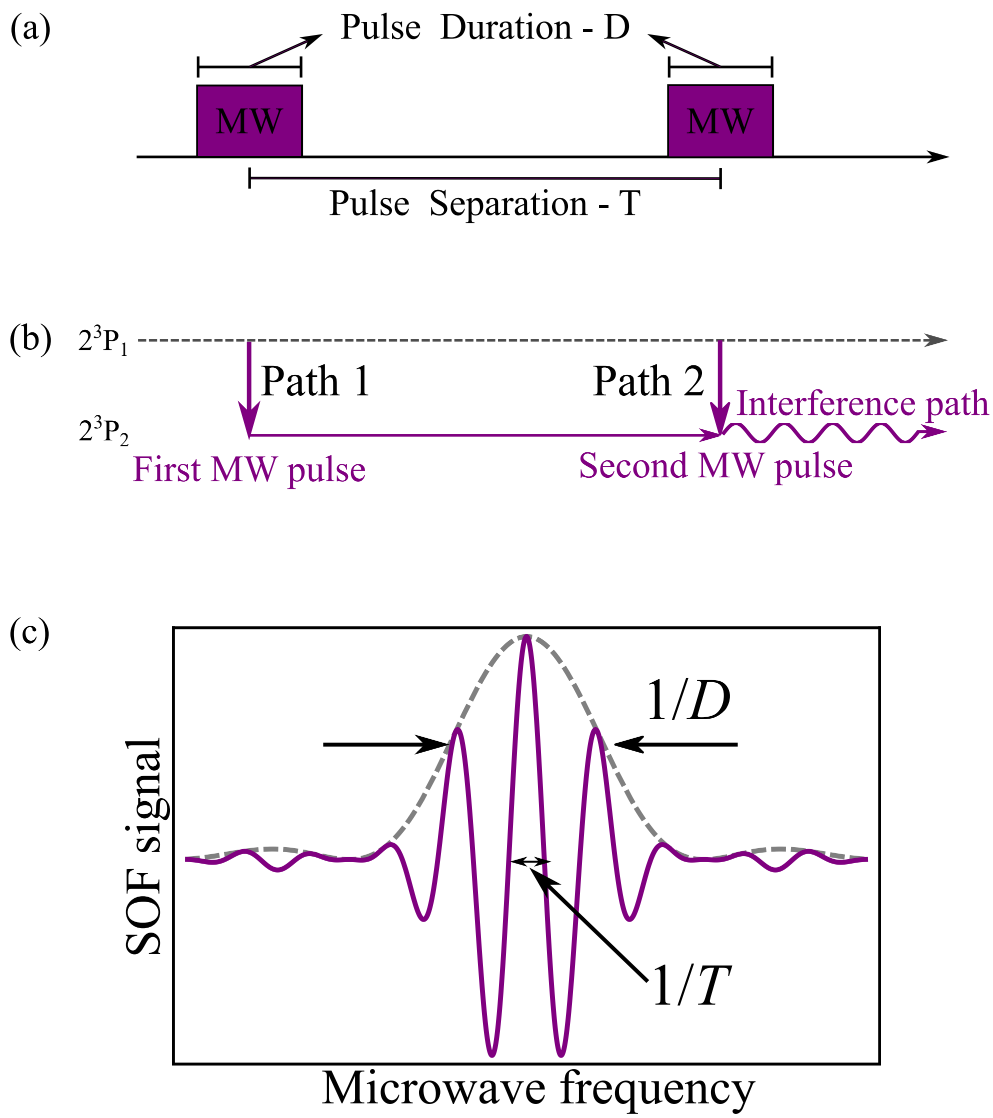

Figure 2.1: The pulse timings of a SOF experiment (a), the two quantum-mechanical amplitudes (b), and the corresponding SOF line-shape (c).

detuning of the applied microwave frequency from the atomic resonant frequency. Equation 2.2 assumes ideal microwave pulses, including instantaneous turn-on and turn-off, no chirp in the phase due to the microwave switches or amplifier, and no changes in intensity or phase profiles as a function of f. The line shape of equation 2.2 is antisymmetric with respect to $\Delta\omega$ (with $\Delta\theta$=0 at $\Delta\omega$=0), and reduces to the very simple proportional relation $\Delta\theta=\Delta\omega T$ for small V. Examples of observed line-shapes are shown in figure 4.2 (a) and (b) for the cases of T=300 ns and D=100 ns with three different values of V (i.e., different powers P).

2.2. Phase Reversal and Line-Shape

To determine the phase difference $\Delta\theta$, the microwaves used for the two pulses are combined and the resulting beat signal is observed. The atomic signals and the beat signal are shown in figure 4.1. Two different timing sequences are used for the measurement: figure 2.2(I), in which the $f+\delta f$ pulse occurs before the $f-\delta f$ pulse, and figure 2.2(II), in which this ordering is reversed.

To switch from (I) to (II), only the timing of the laser pulses is shifted and the microwave pulses remain unchanged. Figure 4.1 shows that the sign of the phase shift $\Delta\theta$ is opposite for the two cases. The quantity

$$\overline{\Delta\theta} = (\Delta\theta_{(\mathrm{II})} - \Delta\theta_{(\mathrm{I})})/2 \tag{2.3}$$

gives the best estimate for $\Delta\theta$ in that it cancels unintended phase shifts in both the atomic and beat signals, as discussed in Ref. [65].

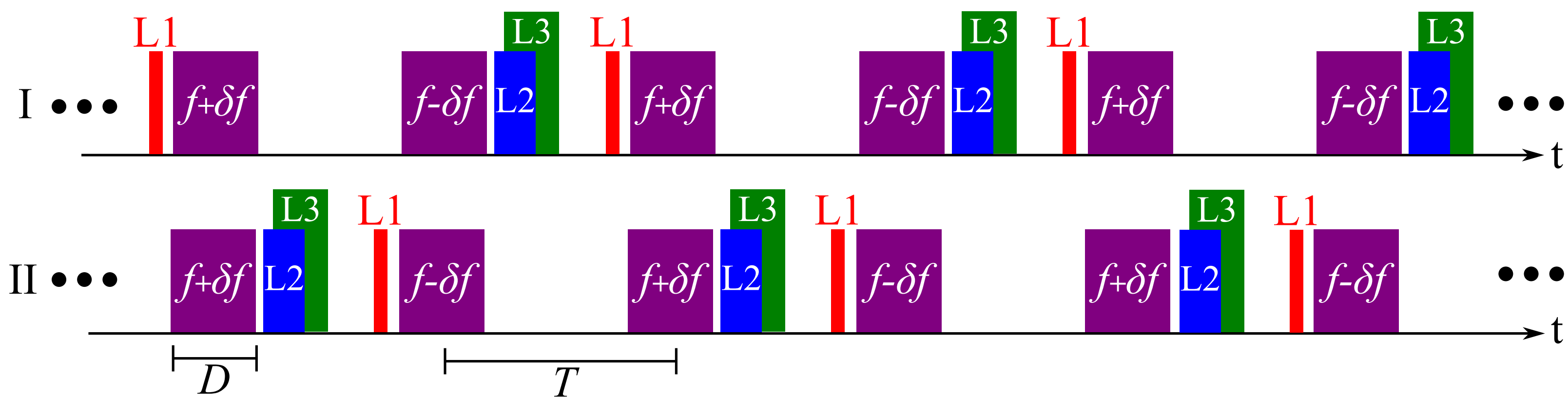

Figure 2.2: The timing of microwave and laser pulses. Each experiment cycle involves laser pulse L1 populating the initial state (2^3P_1), two consecutive microwave pulses being applied, and laser pulses L2 and L3 detecting that the microwave transition is made. For case (I), the first microwave pulse applied has frequency $f + \delta f$, and for case (II), the first microwave pulse has frequency $f - \delta f$.

3. Experimental Apparatus

In this chapter, a general overview of the apparatus is described in the first section, with the following sections providing more detailed descriptions of the sub-components.

3.1. Experiment Overview

For the present experimental setup, most of the components are the same as those used for the 2^3P_2-to-2^3P_1 measurement [69]. A side-view of the experimental apparatus is shown in figure 3.2. Liquid-nitrogen-cooled 2^3S helium atoms (He*) are produced by a DC-discharge source in the source chamber, as described in section 3.2.1. The He* beam is collimated and concentrated by a 2-dimensional magneto-optical trap (2D-MOT), as described in section 3.2.2. Upon entering the experiment chamber, the He* atoms are optically pumped and the FOSOF experiment sequence of figure 2.2 takes place.

The atoms are optically pumped into the 2^3S m=-1 state, or alternatively the m=$+1$ state (as shown in the energy-level diagram of figure 3.1), using a 1083-nm laser beam shown in figure 3.3. The He* then passes through a rectangular microwave waveguide. Inside this waveguide, the majority of the 2^3S(m=-1) atoms are excited by a pulse of 1083-nm laser light (laser L1 in figures 2.2, 3.1, and 3.3) to the 2^3P_1(m=0) state, which has a lifetime of 98 ns. The 1083-nm laser systems are described in section 3.3.1.

The $2^3P_1(m{=}0)\rightarrow 2^3P_0(m{=}0)$ transition is then driven with 29.6-GHz microwaves. The microwave transition is driven by two pulses, each of duration D, and separated in time by T, with a

FOSOF frequency offset of δf (as previously discussed in section 2.1), as shown in figure 2.2. In the approximately 1 μs that it takes for the atoms to pass through the region where the laser beams can interact with the atoms, they typically experience one or two cycles of the timing sequence of figure 2.2. The microwave system is described in more detail in section 3.4.

The $2^3\mathrm{P}_0$ atoms that result from driving the microwave transition are detected by exciting them to the $4^3\mathrm{D}_1$ state using a pulse of 447-nm laser light (L2 in figures 2.2, 3.1, and 3.3), and then to the $18^3\mathrm{P}_2$ state using a pulse of 1532-nm light (L3 in figures 2.2, 3.1, and 3.3). The 447-nm and 1532-nm laser systems are described in detail in section 3.3.2. The $18^3\mathrm{P}_2$ atoms are Stark-ionized by an electric field (see figure 3.3(b)), with the resulting ions collected using ion optics that guide them into a channel electron multiplier (CEM). The signal from the CEM is amplified with a transimpedance current amplifier to obtain the atomic signal. Examples of such signals are shown in figure 4.1.

After passing through the experiment chamber, the He* beam passes through the 1532-nm locking chamber (see figure 3.2). This chamber is used to lock the frequency of the 1532-nm laser. The He* beam continues through the Stern-Gerlach chamber (see figure 3.2), where a Stern-Gerlach magnet is used to split the He* beam into three beams consisting of the $m = 0$ and $m = \pm 1$ populations. A chopper at the beginning of this chamber enables a time-of-flight (TOF) measurement, from which the He* beam's velocity distribution can be determined, as further discussed in section 5.3.

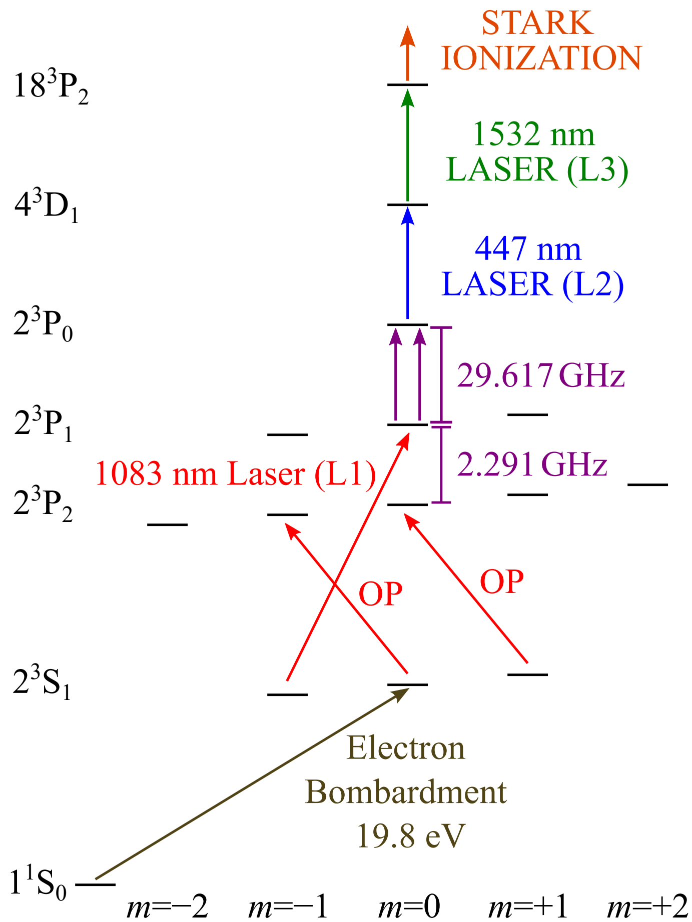

Figure 3.1: A helium energy-level diagram (not to scale), shows the 29.617-GHz interval being measured and all states involved in optical pumping (OP), laser excitation (L1, L2, and L3), and ionization.

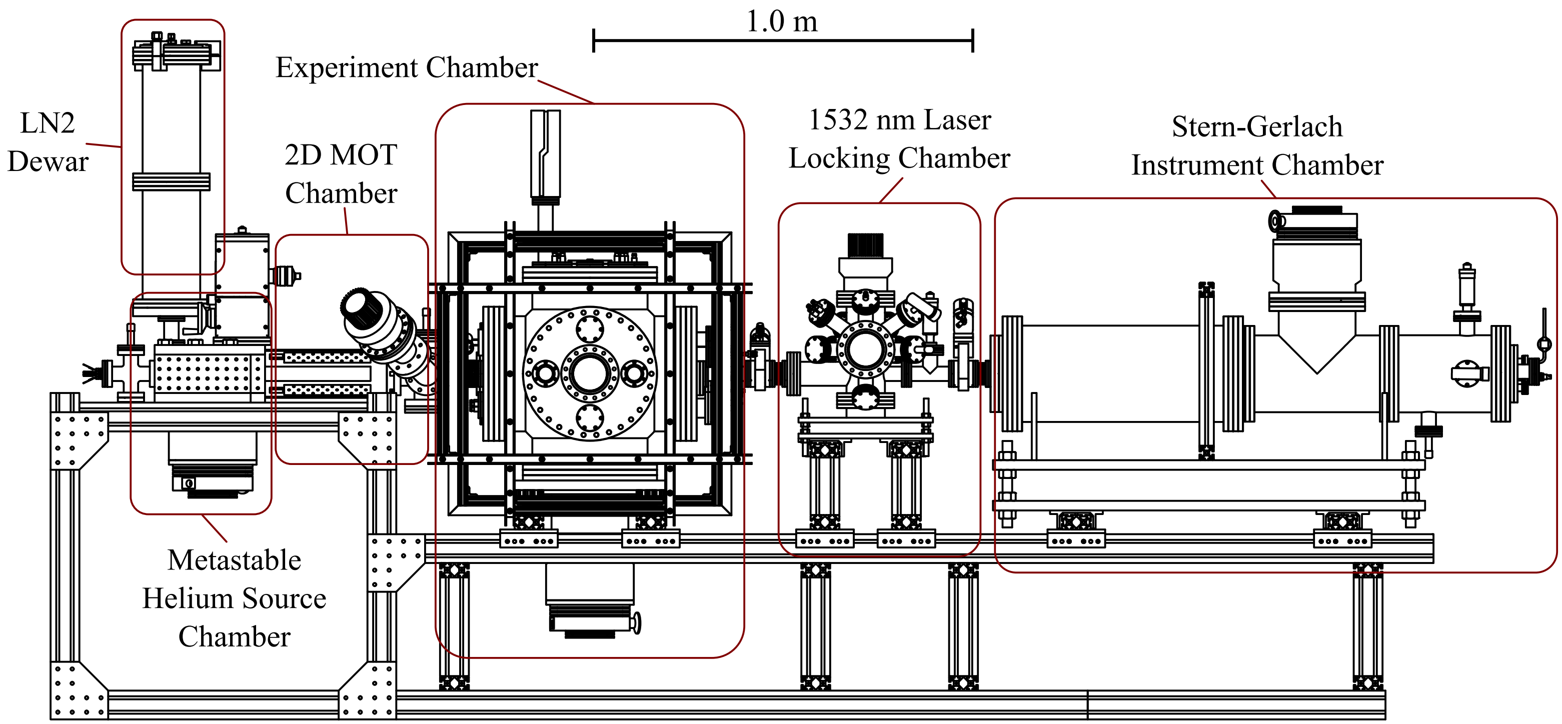

Figure 3.2: Side-view of the apparatus used in the experiment (drawn to scale), with major sections labelled.

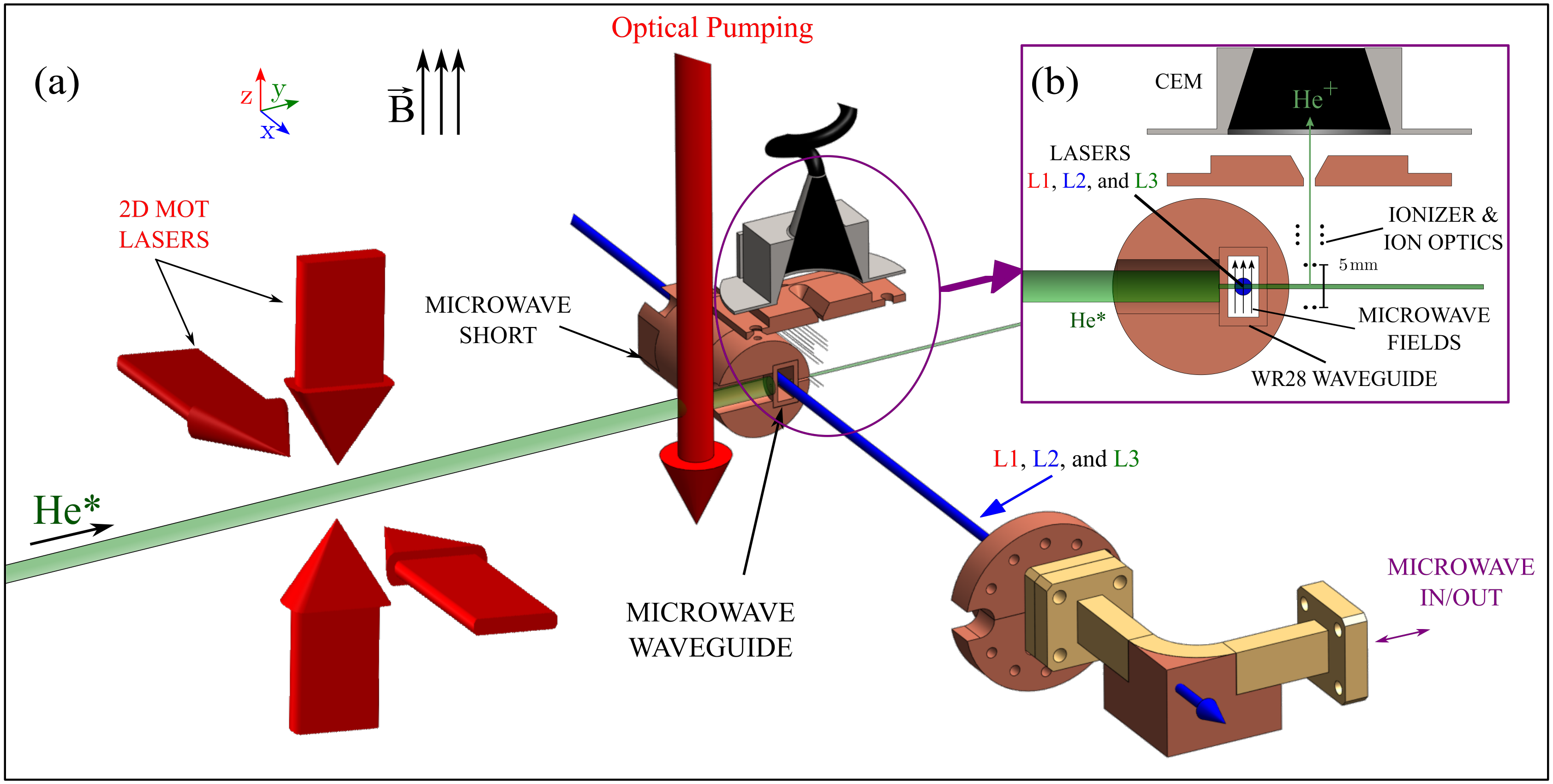

Figure 3.3: A schematic of the experimental layout (a), along with an expanded view of the region where the measurement takes place (b). The green beam indicates the path of the helium atoms, which get excited to the 18^3P_2 state with laser (L1, L2, and L3) and microwave pulses. They are ionized, with the He^+ ions being guided into the CEM by the ionizer and ion optics, respectively, to produce the FOSOF atomic signal.

3.2. Metastable Helium Beam Generation and Conditioning

The metastable helium source section, where metastable He* atoms are generated, and the 2D-MOT section, where the He* beam is collimated and intensified, are discussed below.

3.2.1. Metastable Helium Source

The metastable helium (He*) source generates He* atoms using a liquid-nitrogen-cooled DC-discharge source in the source chamber. The source (see figure 3.4) consists of a high-voltage tungsten needle, centred on the inside of an alumina tube, and a boron-nitrite cap attached to the tube with a 0.3-mm-diameter exit hole out of the source, also concentric to the needle. Approximately 15 mm downstream from where the helium exits this cap is a grounded skimmer, which has a continuous dc discharge of 25 mA between it and the needle. This discharge excites helium atoms that flow through the cap and generates metastable helium atoms. A helium flow rate of approximately 100 standard cubic centimetres per minute (sccm) leads to a pressure of approximately 30 torr in the alumina tube. The same exit hole, along with a 10-inch turbo-pump in the source region, leads to a pressure of $4.5 \cdot 10^{-5}$ torr in the source vacuum chamber.

A dewar of liquid-nitrogen (shown in figure 3.4) is integrated into the source vacuum chamber and is connected via copper braids to a copper clamp holding the alumina tube and the boron nitride cap. This system brings the temperature of the source down to 135 K. The small exit hole in the boron-nitride cap ensures that the helium atoms collide with its walls, cooling and hence slowing them down to a mean speed 1100 m/s. The cooled helium beam then passes through the grounded skimmer and into the magneto-optical trap section for collimation.

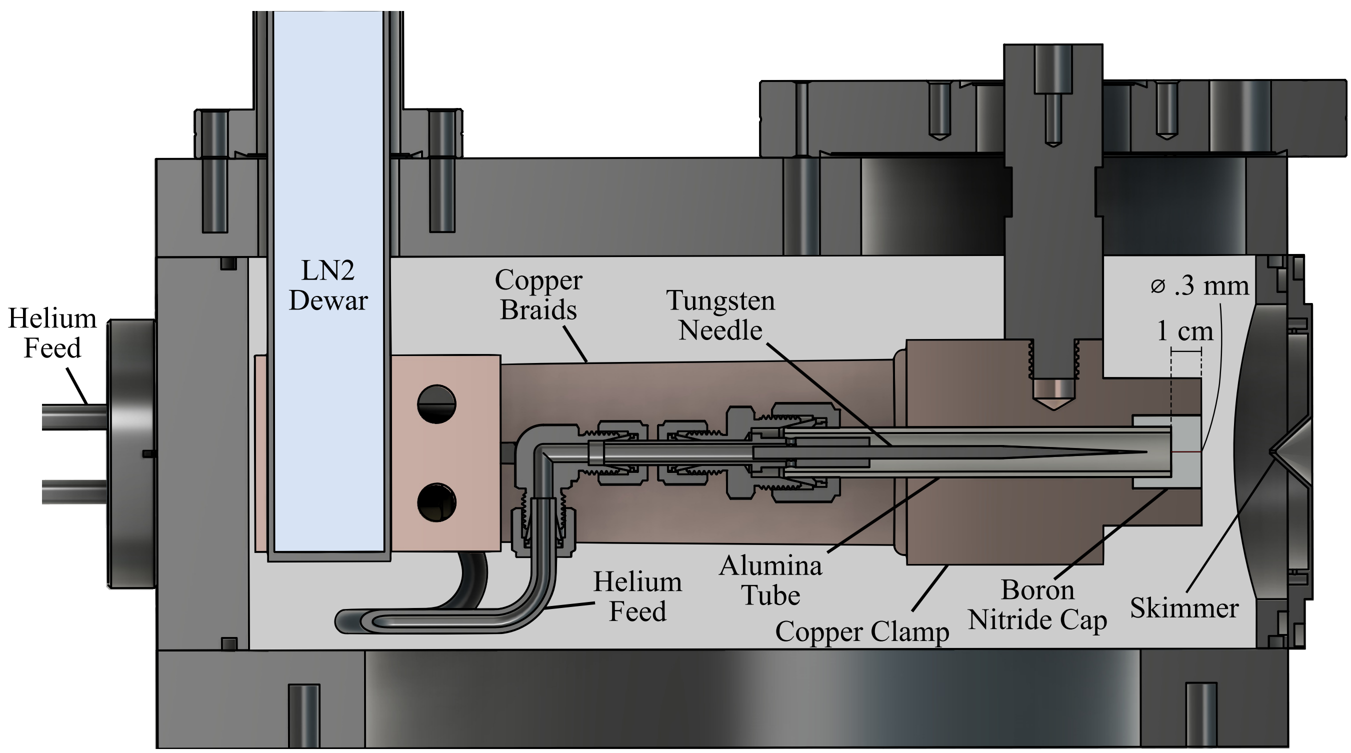

Figure 3.4: Cross-sectional view of the metastable helium source assembly (drawn to scale), with the components of the source labelled and the dimensions of the boron nitride exit hole shown.

3.2.2. Two-Dimensional Magneto-Optical Trap

The 2D-MOT vacuum chamber, which can be seen in figure 3.2, consists of an approximately 32-cm-long cylindrical vacuum tube with windows on the top, bottom, left, and right sides, and permanent bar magnets positioned at the diagonal corners (as shown in figure 3.5). The MOT has two stages, with each stage using a pair of 1083-nm laser beams (generated as described in section 3.3.1) passing through the windows of the chamber, as shown in figure 3.5. The bar magnets generate a magnetic field gradient with a magnetic field of $B = 0$ approximately on the centre axis of the chamber, and with increasing $|B|$ farther away radially from the centre axis. These magnets cause the He* atoms passing through the chamber to experience a greater Zeeman shift the farther away that they are from the centre. In addition to the Zeeman shift, atoms with a velocity component parallel to a laser beam experience a Doppler shift. By detuning the laser to the red of the atomic resonant frequency (as described in section 3.3.1), one can ensure that the 2D-MOT laser beams are closer to resonance for atoms experiencing greater Doppler or Zeeman shifts. As a result, the atoms whose positions are farther from the magnetic-field zero and the ones that have velocities with greater radial components are forced into a collimated atomic beam by the laser beams. The first stage of the 2D-MOT begins immediately following the source skimmer, maximizing the number of He* atoms captured by the 2D-MOT, while the second stage further intensifies the atomic beam. The two stages intensify the He* beam to a measured flux of $7 \times 10^{12}/\mathrm{cm}^2/\mathrm{s}$ and result in a boost to the FOSOF signal by about a factor of 25.

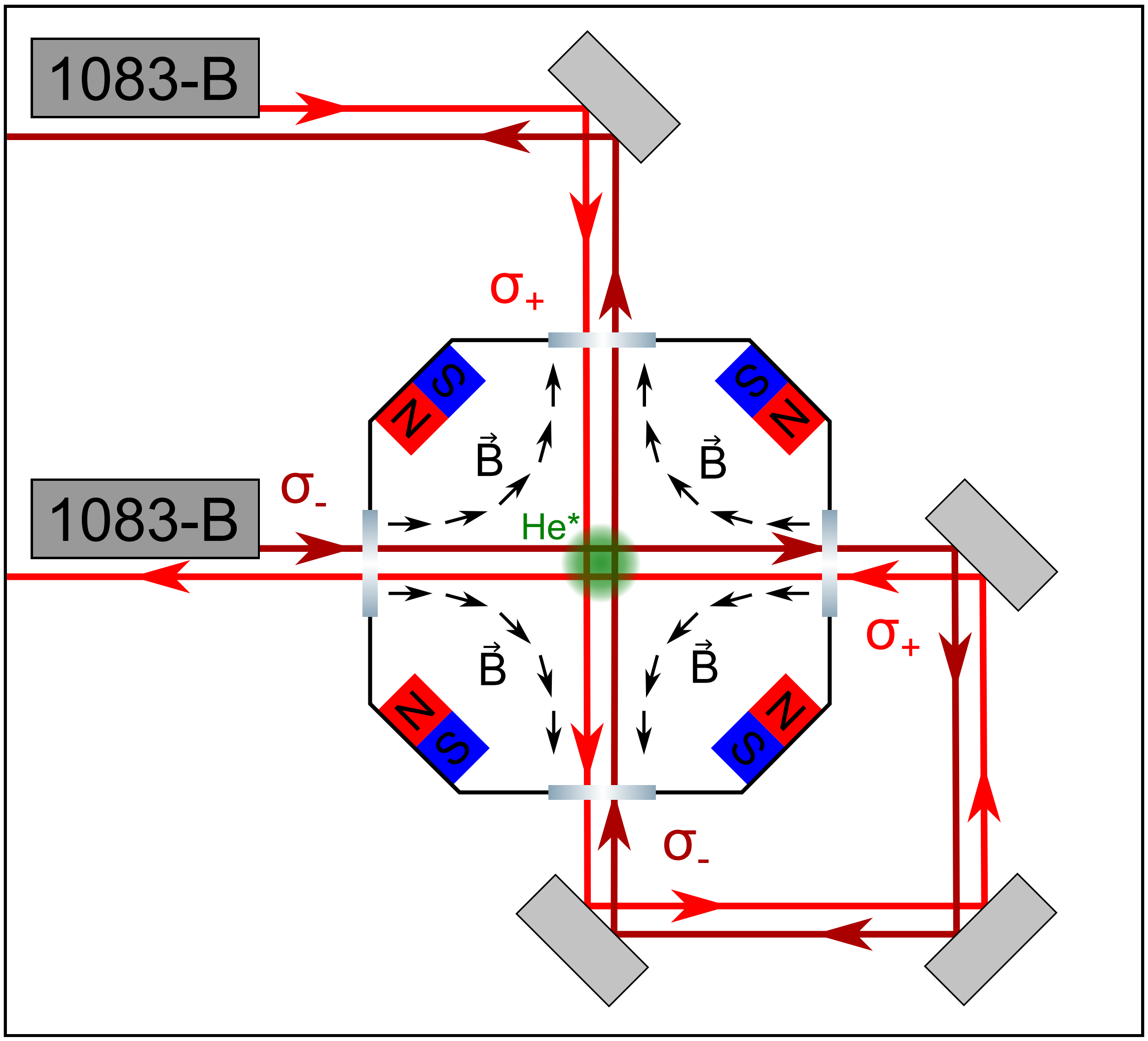

Figure 3.5: Cross-sectional view of the 2D-MOT vacuum chamber. The 1083-nm 2D-MOT laser beams (labelled 1083-B) are generated as shown in figure 3.7.

3.3. Laser Systems

There are five lasers used in the experiment: three with a wavelength of 1083 nm, which drive 2^3S_1-to-2^3P_J transitions, one with a wavelength of 447 nm, which drives the $2^3\mathrm{P}_0$-to-$4^3\mathrm{D}_1$ transition, and one with a wavelength of 1532 nm, which drives the 4^3D_1-to-$18^3\mathrm{P}_2$ transition.

3.3.1. 1083-nm Lasers

The first 1083-nm laser, referred to as 1083-A, is used to drive the transition from $2^3\mathrm{S}_1$ to $2^3\mathrm{P}_1$ (laser L1 in figures 2.2 and 3.3). The second 1083-nm laser, referred to as 1083-B, drives transitions from $2^3\mathrm{S}_1$ to $2^3\mathrm{P}_2$ and is used both in the 2D-MOT and for optical pumping. The third 1083-nm laser, referred to as 1083-C, drives transitions from $2^3\mathrm{S}_1$ to $2^3\mathrm{P}_1$ and is used to generate locking signals to frequency stabilize the 447-nm and 1532-nm lasers. All three 1083-nm lasers use the same model of distributed-Bragg-reflector (DBR) laser diode (Photodigm PH1083DBR), powered by the same model of laser driver (Melles Griot 06DLD203A).

The 1083-A output is split into two beams; the first beam is used for frequency stabilization and the second one is amplified to 500 mW using a fibre amplifier (as shown in figure 3.6). To generate the pulses required for FOSOF, the amplified beam goes through two acousto-optic modulators (AOM), each with a double pass. Before each double pass, the beam is passed through a half-wave plate ($\frac{\lambda}{2}$) in figure 3.6 and polarizing beam-splitter (PBS) pair to set its power and polarization (as detailed in figure 3.6). For the double pass, a linearly polarized beam is sent into the AOM for a first pass, with the laser-beam alignment set to maximize the power in the first-order diffracted beam. The retroreflection of the first-order diffracted beam is returned into the AOM for a second

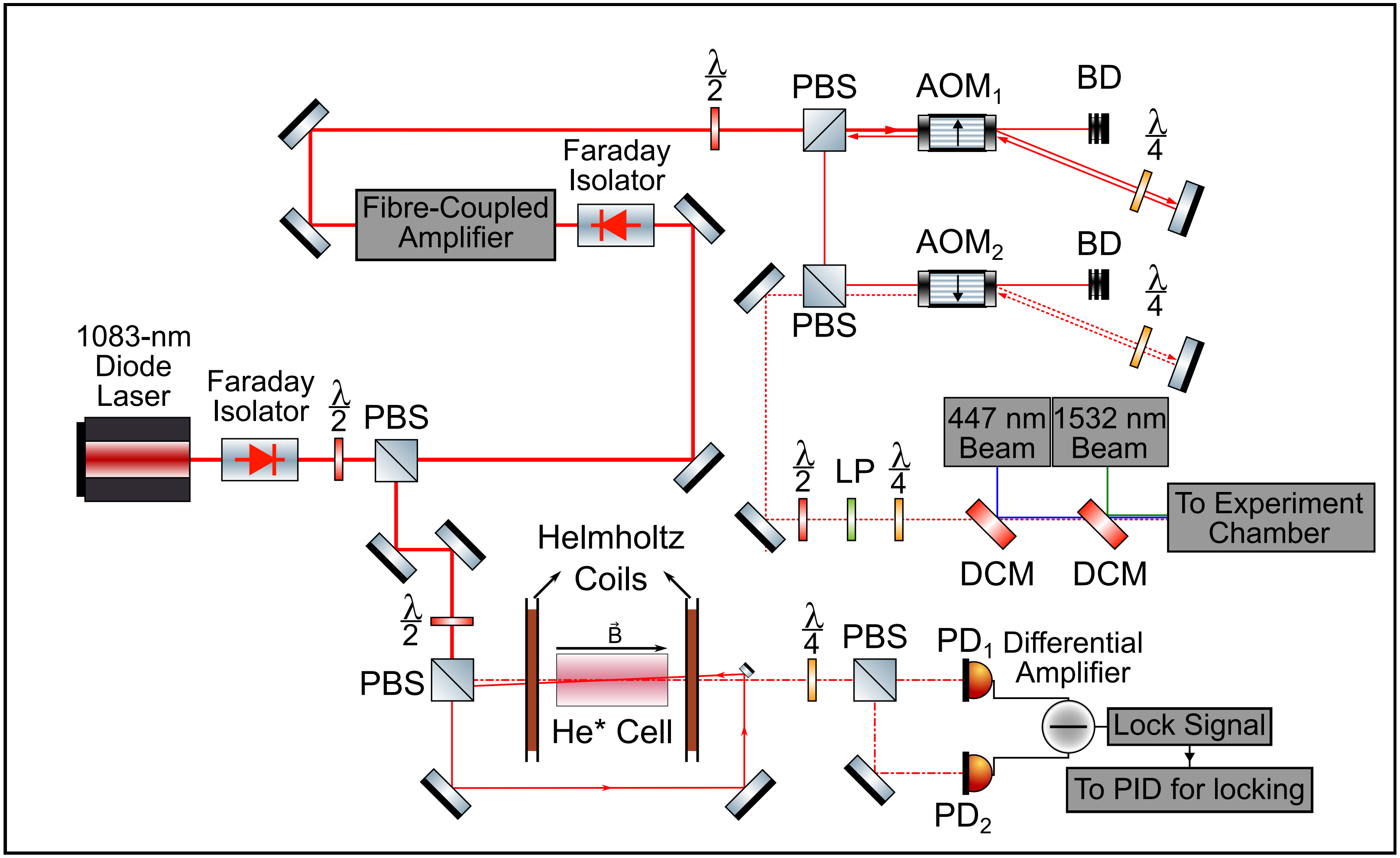

Figure 3.6: Schematic representation of the optics and optical paths for the 1083-A laser system. Components are labelled as follows: $\frac{\lambda}{2}$: half-wave plate, $\frac{\lambda}{4}$: quarter-wave plate, LP: linear polarizer, BD: beam dump, PBS: polarizing beam-splitter, BS: beam-splitter, DCM: dichroic mirror, PD: photo-detector, AOM: acousto-optic modulator. This figure has been made using modified and unmodified assets from the component library in reference [70].

pass. The first-order diffracted beam of the second pass travels antiparallel to the initial beam and has a frequency shift of of twice the RF frequency driving the AOM. By placing a quarter-wave plate ($\frac{\lambda}{4}$ in figure 3.6) between the AOM and the mirror that reflects the beam back into the AOM, one ensures a $\frac{\pi}{2}$ rotation of the polarization axis for the final beam, which allows it to pass through rather than get reflected by the polarizing beam-splitter (labelled PBS in figure 3.6).

The double-pass configuration is used to fine-tune the frequency of the laser beam, which allows it to target atoms in either the $2^3\mathrm{S}_1$ $(m_J = +1)$ or $2^3\mathrm{S}_1$ $(m_J = -1)$ state. In addition, it enables generation of nanosecond-scale pulses (see, e.g., the pulses in figure 2.2) more precisely than a single-pass configuration could, as the rise and fall times are sharper. The pulse shaping is performed by switching the RF input driving the second AOM (AOM_2 in figure 3.6) while the first AOM (AOM_1 in figure 3.6) is driven continuously. AOM_1 applies a frequency up-shift and AOM_2 applies a frequency down-shift to the beam.

The 1083-B laser beam is amplified to approximately 2 watts with a fibre amplifier and split into three beams, as shown in figure 3.7. The first beam (with most of the power) is used for the 2D-MOT, the second beam is used for optical pumping, and the third beam is used to frequency-stabilize (i.e., lock the frequency of) laser 1083-B. The locking beam double-passes through two AOMs, as shown in figure 3.7. The first AOM down-shifts and the other up-shifts the frequency, applying a combined frequency offset of approximately -20 MHz. This offset results in the other two beams being detuned approximately 20 MHz off of resonance when the locking beam is locked to the atomic resonance centre. This red detuning is required for the 2D-MOT, as discussed in section 3.2.2. The 2D-MOT laser beam is split into four beams, which are circularly polarized and pass through a horizontal cylindrical beam expander, before being sent to the 2D-MOT vacuum chamber

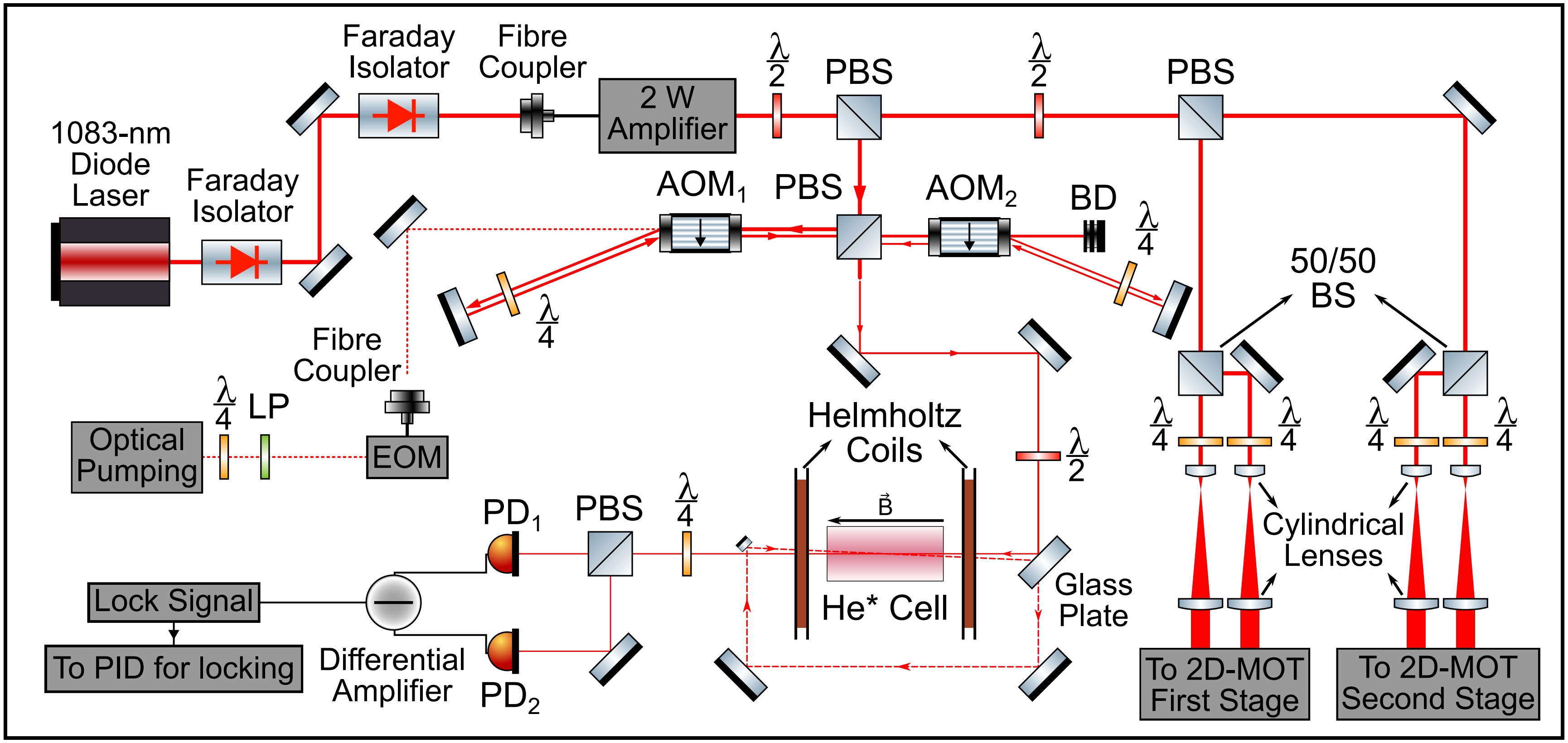

Figure 3.7: Schematic representation of the optics and optical paths for the 1083-B laser system. Components are labelled as follows: $\frac{\lambda}{2}$: half-wave plate, $\frac{\lambda}{4}$: quarter-wave plate, LP: linear polarizer, BD: beam dump, PBS: polarizing beam-splitter, BS: beam-splitter, PD: photo-detector, AOM: acousto-optic modulator, EOM: electro-optic modulator. This figure has been made using modified and unmodified assets from the component library in reference [70].

(using the configuration shown in figure 3.5 for each of the two stages).

The optical-pumping laser beam passes through an electro-optic modulator (EOM) before interacting with the He* beam in the experiment chamber. The EOM is used both to compensate for the 20-MHz detuning relative to the locking beam and to add fine-tunable sidebands that are resonant with the optical-pumping transitions $2\,^3\mathrm{S}_1$ ($m = +1$)-to-$2\,^3\mathrm{P}_2$ ($m = 0$) and $2\,^3\mathrm{S}_1$ ($m = 0$)-to-$2\,^3\mathrm{P}_2$ ($m = -1$), or $2\,^3\mathrm{S}_1$ ($m = -1$)-to-$2\,^3\mathrm{P}_2$ ($m = 0$) and $2\,^3\mathrm{S}_1$ ($m = 0$)-to-$2\,^3\mathrm{P}_2$ ($m = +1$) (depending on whether optical pumping is to $2\,^3\mathrm{S}_1$ ($m = -1$) or $2\,^3\mathrm{S}_1$ ($m = +1$), respectively). The optical-pumping beam is circularly polarized using a combination of a fixed linear polarizer and a quarter-wave plate ($\frac{\lambda}{4}$) in figure 3.7 to obtain the polarization required to the drive the transitions. The EOM frequency offsets are set to match the Zeeman shifts caused by the applied magnetic field in the experiment region.

The 1083-A and 1083-B lasers are frequency stabilized using the method of dichroic atomic vapour laser lock (DAVLL), which is a variation of saturated-absorption spectroscopy [71]. Both the 1083-A and 1083-B lasers have dedicated metastable helium RF discharge cells for performing a DAVLL lock. The locking beam from each laser is split, using a PBS, into a pump beam and a probe beam, which counter-propagate through the discharge cell. A magnetic field is applied to each cell with a pair of Helmholtz coils. The resulting Zeeman shift leads to a separation of the $m = +1$ and $m = -1$ Zeeman components of metastable helium atoms in the cell. The pump and probe beams are linearly polarized with a polarization perpendicular to the applied magnetic field. This linear polarization is a combination of σ^+ and σ^- polarizations, and can therefore drive both $\Delta m = +1$ and $\Delta m = -1$ transitions. The absorption signals from both transitions are measured by a pair of photodetectors and subtracted to form an error signal for locking. An analog PID (proportional, integral, and derivative) controller (SRS SIM960) is used to maintain a lock on the centre of the error signal by modulating the output current of the laser drivers to the laser diodes.

The 1083-C laser beam is split into two beams using a $\frac{\lambda}{2}$ plate and PBS pair, as shown in figure 3.8. The first beam is sent to a metastable helium RF discharge cell to lock the frequency of laser 1083-C. The other beam is split with a 50/50 beam-splitter, with the two resulting beams being used to lock the 447-nm and 1532-nm lasers, respectively, as shown in figure 3.8. The locking beam goes through a wedge plate beam-splitter, which reflects two beams of approximately equal power, with most of the power being transmitted through it. The 1083-C lock signal is generated using saturated-absorption spectroscopy. The transmitted beam and one of the two reflected beams (see figure 3.8) are used as the pump and probe beams, respectively, while the second reflected beam is used to measure background signal. The locking signal is formed by subtraction the photo-detector signal of the background beam from that of the probe beam. A lock-in amplifier and a PID controller are used to frequency-stabilize the laser.

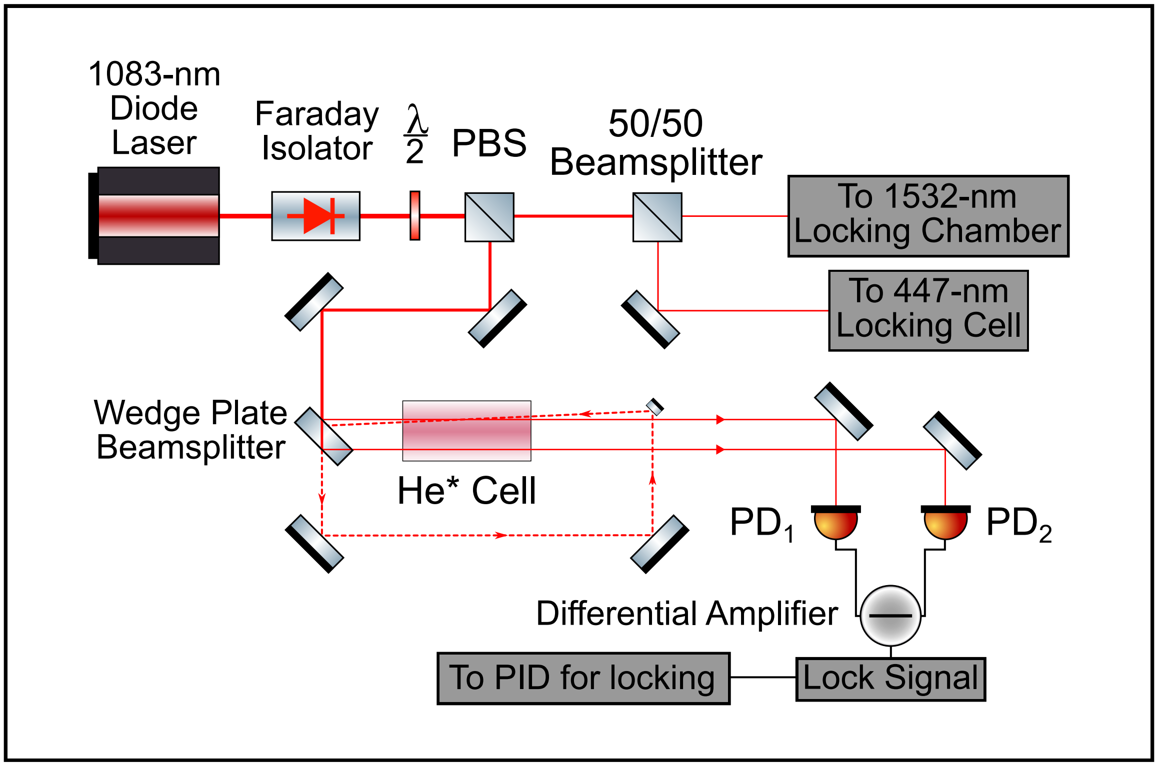

Figure 3.8: Schematic representation of the optics and optical paths for the 1083-C laser system. Components are labelled as follows: $\frac{\lambda}{2}$: half-wave plate, PBS: polarizing beam-splitter, PD: photodetector. This figure has been made using modified and unmodified assets from the component library in reference [70].

3.3.2. Detection Lasers

The 447-nm and 1532-nm diode lasers (laser L2 and laser L3, respectively, in figures 2.2 and 3.3) drive transitions from 2^3P_0 to 4^3D_1 and from 4^3D_1 to 18^3P_2, respectively. They are referred to as detection lasers as together they drive only helium atoms that have made the $2^3P_1$to-2^3P_0 microwave transition into the 18^3P_2 Rydberg state, which are ionized and guided into the CEM.

The 447-nm beam is generated using a Toptica DL-PRO external-cavity diode laser (ECDL) and is split into two beams, as shown in figure 3.9(a). The first beam is used to drive transitions from 2^3P_0 to 4^3D_1 in the main experiment and the other beam is used to lock both the 447-nm and 1532-nm lasers. The experiment beam double-passes through an AOM for frequency fine-tuning and for the fast-switching required to generate the pulses shown in figure 2.2. The locking beam goes through another AOM for frequency tuning and is split into two beams, one to lock the 447-nm laser and the other to lock the 1532-nm laser.

The 447-nm laser is locked using a standard saturated-absorption setup with a metastable-helium discharge cell similar to the ones used to lock the 1083-nm lasers. The 447-nm locking beam is split into two beams using a polarizing beamsplitter, with one used as a probe and the other used to obtain background signal (see figure 3.3.2(a)). The 1083-C beam, counter-propagating with the 447-nm probe beam, serves as the pump beam and drives helium atoms from 2^3S_1 to 2^3P_0, so that the 447-nm beam can excite them to the 4^3D_1 state. The background-subtracted signal from the two photodetectors is sent to the 447-nm laser controller, which locks its frequency using its built-in PID and lock-in amplifier.

The 1532-nm laser beam is produced with a fibre-coupled Alcatel A-1905-LMI distributed-

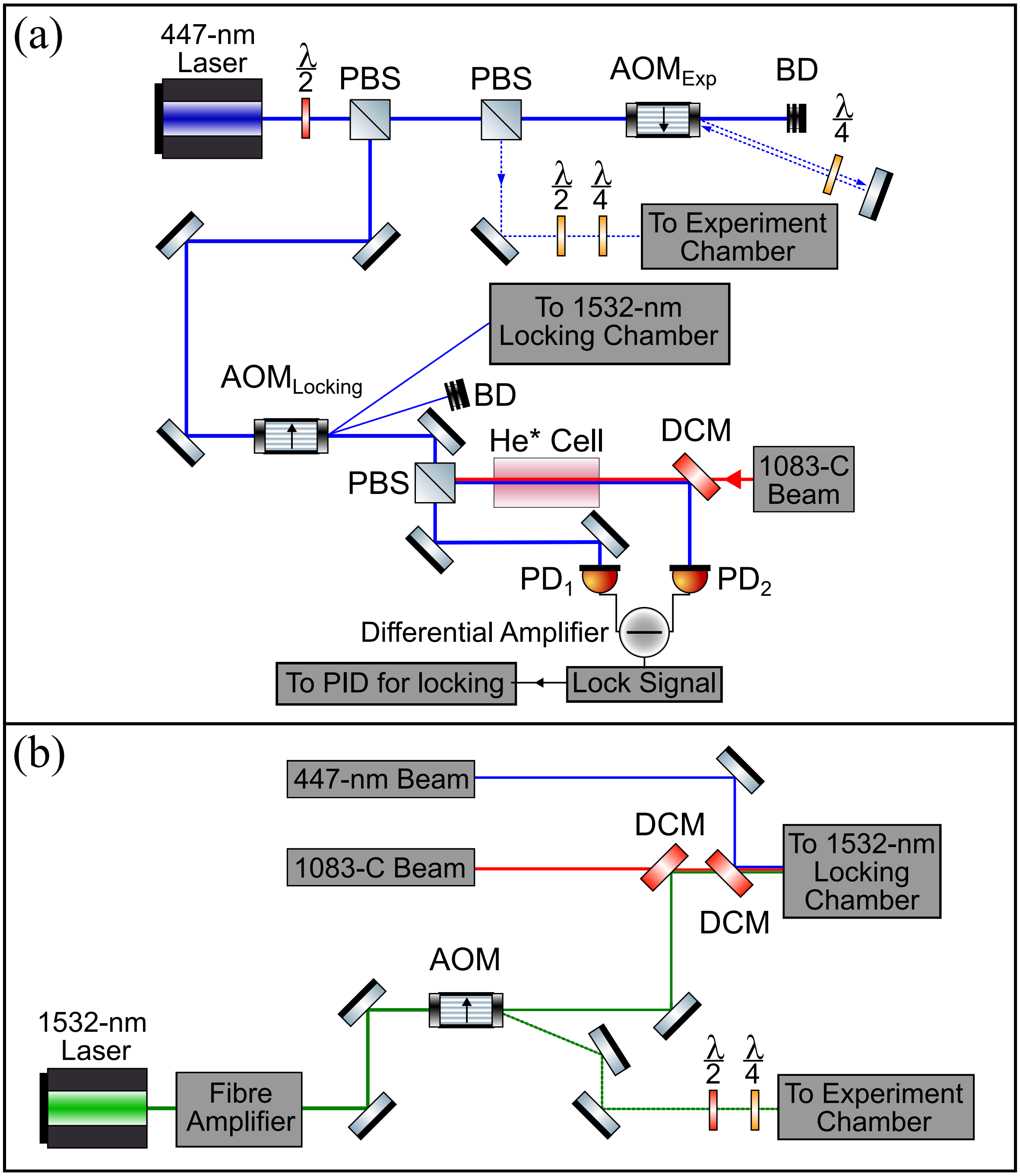

Figure 3.9: Schematic representation of the optics and optical paths for the detection lasers. Panel (a) shows the 447-nm laser system and panel (b) shows the 1532-nm laser system. Components are labelled as follows: $\frac{\lambda}{2}$: half-wave plate, $\frac{\lambda}{4}$: quarter-wave plate, BD: beam dump, PBS: polarizing beam-splitter, DCM: dichroic mirror, PD: photo-detector, AOM: acousto-optic modulator. This figure has been made using modified and unmodified assets from the component library in reference [70].

feedback (DFB) laser, whose output is amplified to approximately 400 mW using a Nuphoton EDFA-CW-1532-PM-SMR-27-17-FCA amplifier. The output of the amplifier (see figure 3.9(b)) passes through an AOM, driven at 200 MHz, with the laser beam aligned through the AOM to maximize the power in the first-order diffracted beam. The first-order diffracted beam is sent to the experiment chamber and the undiffracted beam is sent to the 1532-nm locking chamber. The laser input current is modulated with a 200-MHz RF input using a bias tee to add $\pm$200 MHz sidebands to the laser beam. The locking signal generated in the 1532-nm locking chamber uses the undiffracted beam, which has no AOM shift applied, and has features due to these $\pm$200-MHz sidebands. The lower sideband compensates for the 200-MHz AOM shift applied to the experiment beam.

The 1532-nm laser is locked using a signal derived from He* atoms from the beam in the 1532-nm laser locking chamber shown in figure 3.2. These atoms are excited from $2\,^3\mathrm{S}_1$ to $2\,^3\mathrm{P}_0$ using the 1083-C laser, from $2\,^3\mathrm{P}_0$ to $4\,^3\mathrm{D}_1$ using the 447-nm laser, and from $4\,^3\mathrm{D}_1$ to the $18\,^3\mathrm{P}_2$ Rydberg state using the 1532-nm laser. These $18\,^3\mathrm{P}_2$ atoms are Stark-ionized and detected using a CEM. The three laser beams used for locking the 1532-nm laser are combined and guided (see figure 3.9(b)) into the 1532-nm locking chamber (see figure 3.2), which is downstream from the experiment chamber (see figure 3.2). The signal generated by the CEM is amplified and sent to a PID to lock the 1532-nm laser.

3.4. Microwave System

Microwaves for the experiment are produced by two precision microwave generators: an HP 83640A and a Wiltron (Anritsu) 68369A/NV. The internal clocks of the generators are locked to each other and referenced to both Rb and GPS clocks. One generator produces the $f+\delta f$ microwaves and the other produces the $f-\delta f$, as shown in figure 3.10. The microwave outputs from the generators are sent to directional power splitters (Marki microwave C13-0140) which split the power with a 95%-to-5% ratio (labelled -13 dB DC in figure 3.10). The smaller portion from each splitter passes through two isolators (Fairview Microwave SFI2731, each of which has a reported minimum isolation of 20 dB). These isolators prevent reflected microwave power from returning to the directional couplers and leaking into the rest of the microwave system. The isolators used for the microwave power from the HP generator are labelled ISO-1A and ISO-2A and the isolators used for the microwave power from the Wiltron generator are labelled ISO-1B and ISO-2B in figure 3.10.

The microwaves leaving the isolators are combined in an RF-Lambda RFLT2W6G40G power combiner (labelled PC-1 in figure 3.10), with a reported insertion loss of 0.7 dB and a typical isolation of 19 dB. The combined microwaves form a beat-note, which is measured by a zero-bias Schottky diode power detector (Krytar Model 203BK) labelled PD_{ref} in figure 3.10. This beat signal is used as the reference signal for determining the (time-varying) relative phase of the two microwave sources. The remaining power from each directional splitter (the 95% arms) goes to a temperature-stabilized switching box, where it passes through two consecutive fast switches (labelled SW1A, SW2A, SW1B, and SW2B in figure 3.10), which produce the microwave FOSOF pulses. SW1A and SW1B in figure 3.10 are Quinstar QSC-AS000Z SPST (single-pole, single-throw) switches (with a reported isolation of 50 dB), while SW2A and SW2B in figure 3.10 are Quinstar QSC-AD000Z SPDT (single-pole, double-throw) switches (with a reported isolation of 50 dB), providing a combined isolation of 100 dB for each switching path between the on and off states. The output of both switching paths are combined in a power combiner labelled PC-2 (RF-Lambda RFLT2W6G40G) and pass through a 6-dB attenuator (before entering the amplifier) which attenuates the power of any reflections between the amplifier input and the power combiner output. The microwave power exiting the 6-dB attenuator is amplified to a power of $P \leq 2$ W.

The amplified microwaves pass through a 2.92-mm coax-to-WR-28 waveguide adapter (Quinstar QWA-28S29F00), followed by a waveguide isolator (Pamtech RYG2031) to prevent reflected microwave power from returning into the amplifier, and a 20-dB directional coupler (HP R752D) [68], which does not affect the forward-travelling microwaves, but splits off a -20-dB sample of microwaves reflected from the rest of the microwave system. The microwaves then enter a WR-28 rectangular waveguide (see figure 3.3), which has inner dimensions of 7.112 by 3.556 mm. This waveguide has 0.5-mm-diameter holes through which the He* beam enters and exits. The waveguide is terminated in a solid-copper electrical short situated one half wavelength from the axis of the 0.5-mm holes. This short reflects the microwaves, creating a standing wave between the incoming and reflected microwaves. This standing wave has a node of electric field and anti-node of magnetic field at the centre of the 0.5-mm holes, through which the He* passes. This positioning minimizes Stark shifts due to the microwave electric fields and maximizes the microwave magnetic-field intensity driving the transition under study.

One percent of the reflected microwave power is split off by a directional coupler (labelled PC-3 in figure 3.10) and is directed into two power detectors. The remainder of the power is absorbed by an isolator (labelled ISO-3 in figure 3.10). The signal from the first power detector (PD_{pulse}) is observed on an oscilloscope (Tektronix DPO7354) to monitor the timing and power of the microwave pulses. The signal from the second power detector (PD_{power}) is monitored on a data logger and it is used to measure the microwave power applied in the experiment.

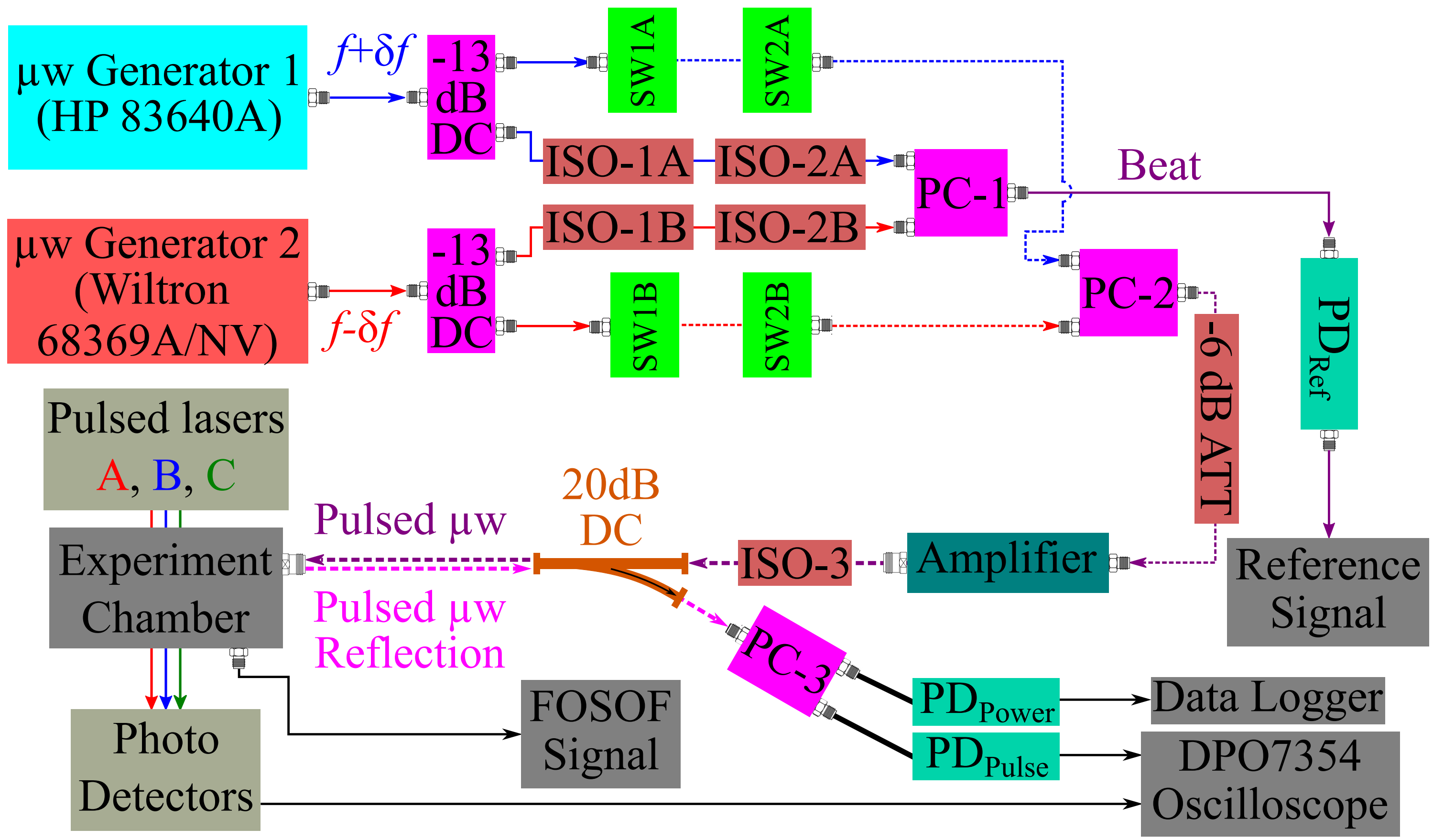

Figure 3.10: The microwave switch setup used to generate FOSOF pulses is shown, with a pair of switches for the $f+\delta f$ pulse (SW1A and SW2A) and $f-\delta f$ pulse (SW1A and SW2A). Components in the figure are labelled as follows: PC: power combiner/splitter, μw: microwave, PD: power detector, SW: switch, DC: directional coupler, ATT: attenuator, and ISO: isolator.

Given the complexity of the microwave system, microwave pulses generated by both generators needed to be calibrated so that they are of equal power (referred to here as power equalization), are constant in power as the microwave frequency is varied within the frequency range of the experiment (referred to here as power flatness), and have power that is proportional to the requested power setting (referred to here as power linearization). The first step in this calibration process is to measure the output of one generator (HP in this case) at a large range of power settings at a single frequency (29,617 MHz) near the centre of the atomic resonance. These power measurements are performed using an HP 436A power meter with an HP R8486A thermocouple waveguide power sensor.

This data can be used to generate a linearization curve from which one can derive the front-panel power settings required on the HP generator to generate output powers of 5 to 100 percent (of the maximum power chosen for the experiment), in 5 percent steps. These front-panel power settings are then applied to both generators at frequencies ranging over 29617 ± 25 MHz. The resulting output powers are shown in figure 3.11(a). After correcting the front-panel settings for the frequency response for each generator, the calibrated output powers, measured for all frequency-power-generator combinations (shown in figure 3.11(b)), have a maximum discrepancy of $.1\%$ from the desired power output, with respect to power equalization, flatness, and linearization.

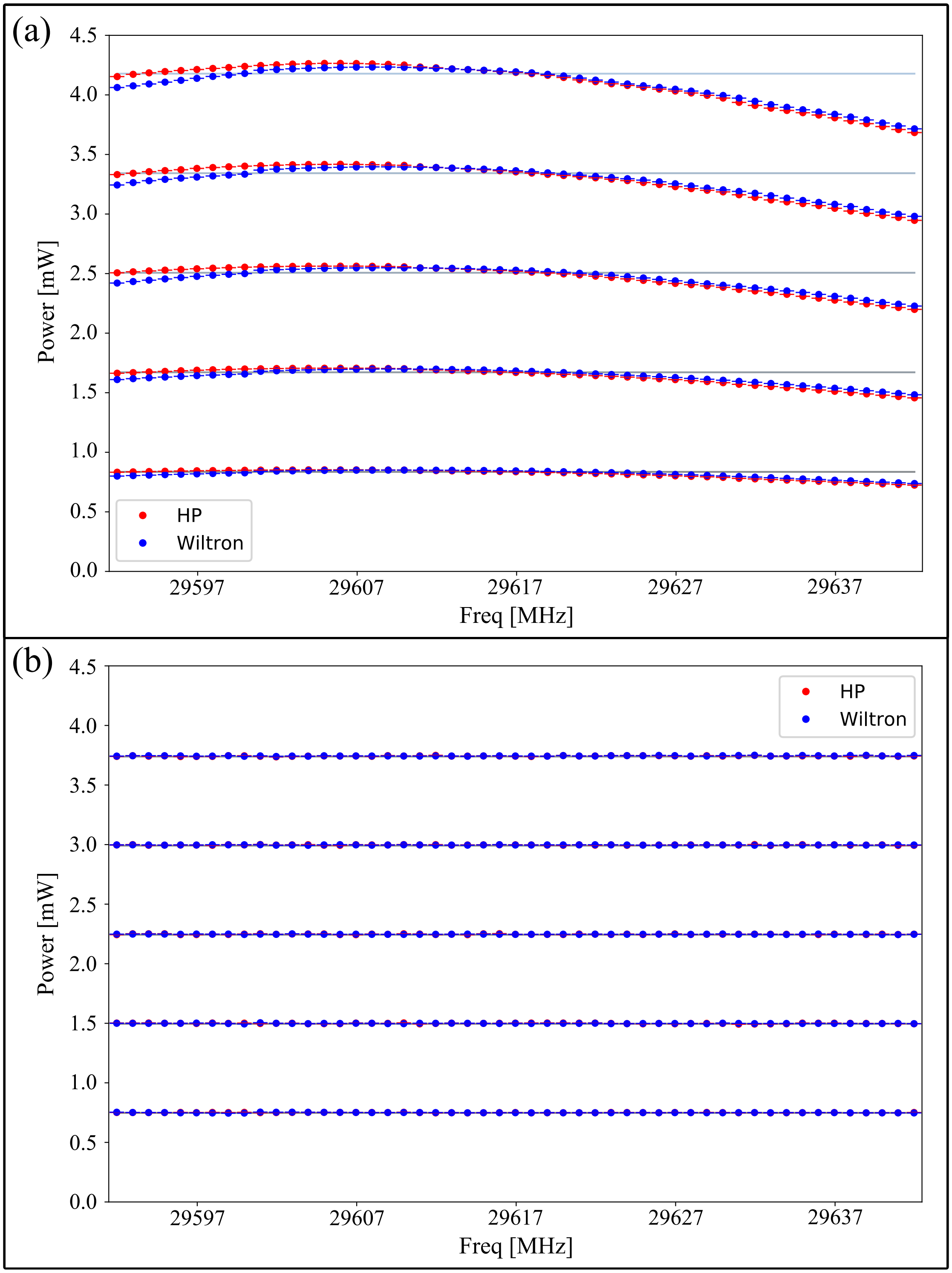

Figure 3.11: Microwave calibration. Panel (a) shows microwave power measured before calibration, while panel (b) shows the measured power after calibration.

4. Data Collection and Analysis

In this chapter, the process of data collection and the analysis to determine the linecentre is discussed.

4.1. Data Collection

The measurement of the $2\,^3\mathrm{P}_1$-to-$2\,^3\mathrm{P}_0$ interval presented in this work includes 8894 data runs taken during six months of data collection. These runs include 680 unique combinations of experimental parameters that are varied to test for systematics. The parameters that are varied are microwave pulse separation (T) and duration (D) (see figures 2.1(a) and 2.2), DC magnetic field (B), microwave power (P), initial 2^3S m-state ($m = -1$ or $m = +1$), and offset frequency. Measured linecentres and uncertainties for specific parameter values are shown in table 5.1 and figure 5.1). The full set of data is reduced to 680 data subsets, each representing the weighted average of the subset of data for each unique combination of experimental parameters. This full set of condensed experimental data is given in Appendix A.1.

For each run of the experiment the atomic and reference (beat) signals (sample signals seen in figure 4.1) are recorded using a two-channel digitizer (Agilent L4534A) for both pulse timings (I) and (II) shown in figure 2.2. This process is repeated for 41 microwave frequencies, one near resonance and 20 symmetrical pairs of frequencies on either side of the resonance. The order in which the frequencies are applied is randomized for each run. Thus, there are 82 atomic signals and 82 corresponding reference signals for each run. Each run is used to determine a centre frequency, as described in section 4.2. Runs that do not have a large enough signal-to-noise ratio for unambiguous

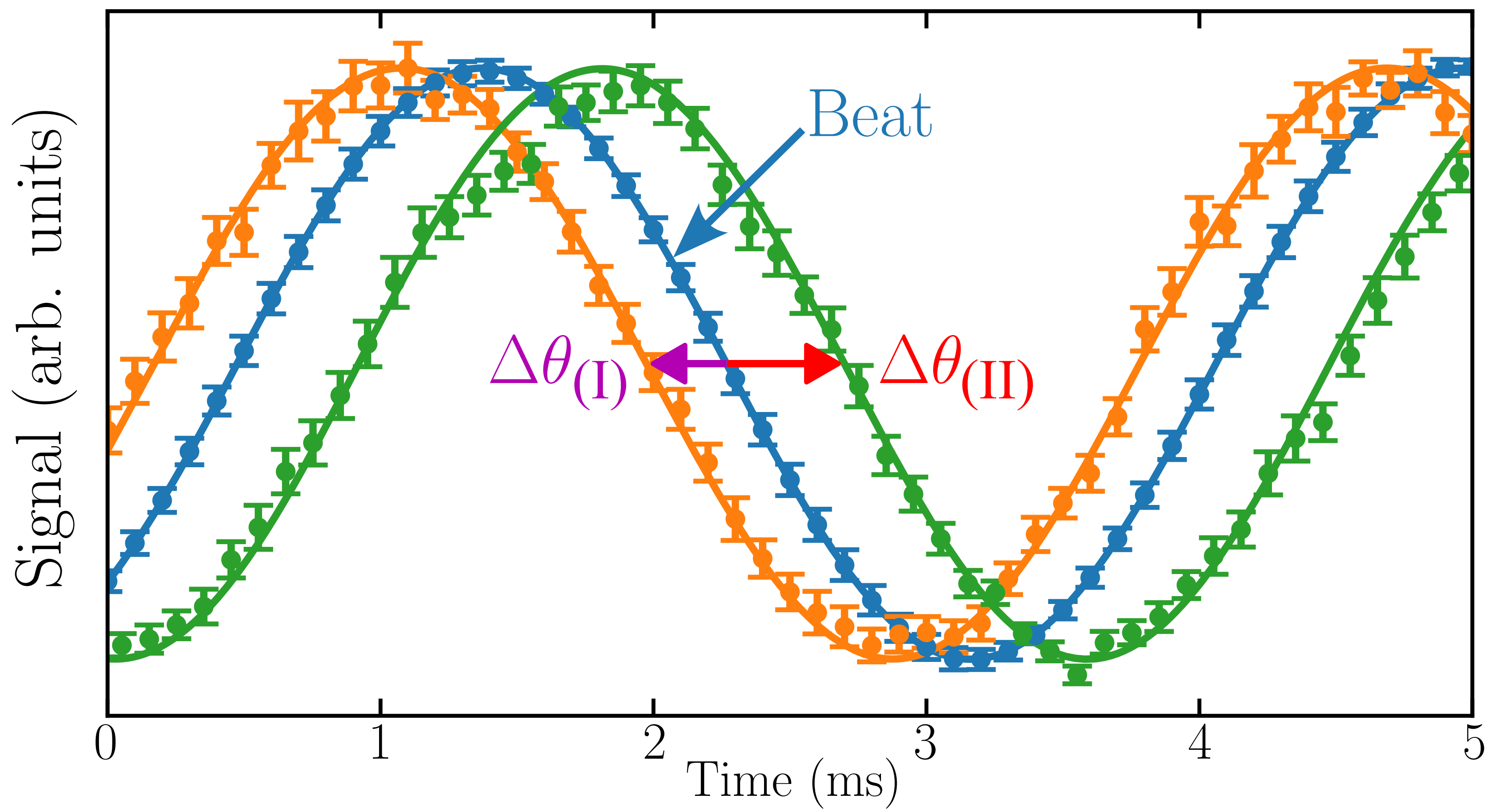

Figure 4.1: A small sample of FOSOF signals for data taken with T = 300 ns and D = 100 ns at 100% power (corresponding to V=2.03 rad/s). The sinusoidal atomic signals for the configurations of figures 2.2(I) and 2.2(II) are shifted by $\Delta\theta_{\mathrm{(I)}}$ and $\Delta\theta_{\mathrm{(II)}}$ relative to a microwave beat signal.

phase determination for all 82 signals are excluded.

In addition to the 680 data subsets, additional data are taken to test for systematic effects. This data includes runs for which individual laser powers are reduced, runs in which the microwave transition from $J = 0$ to $J = 1$ (rather than $J = 1$ to $J = 0$) is driven, runs in which the helium atoms are excited to the 18F state (rather than the 18P state) with the 1532-nm laser prior to Stark ionization, runs with increased source temperature (by cooling with an ice-water bath instead of with liquid nitrogen), and runs in which the linear polarization of the 2^3S-to-2^3P laser is misaligned. Centres and uncertainties for each of these datasets are given in table 5.2 and figure 5.2. These additional data runs are all taken with a pulse separation of 300 ns, a pulse duration of 100 ns, and at the highest microwave power. These datasets serve only as tests for systematic effects and are not included in the weighted average of results used in the calculation of the final measurement result.

4.2. Line-Centre Determination

The process of determining the linecentre for a data run begins with finding the phase difference between the atomic signal and the reference signal using the inner product of both signals with cosine and sine functions at the the FOSOF frequency. The phases found for configurations (I) and (II) of figure 2.2 are then subtracted and divided by two to get $\overline{\Delta\theta}$, the FOSOF phase, as indicated in equation 2.3. This process results in a relative phase determination for each of the 41 microwave frequencies used in the data run.

Four ranges of microwave frequencies are defined: Fr0 ($|f - f_0| \leq \frac{3}{4D}$, with 41 frequencies), Fr1 ($|f - f_0| \leq \frac{1}{2D}$, with 35 frequencies), Fr2 ($|f - f_0| \leq \frac{1}{4D}$, with 29 frequencies), and Fr4

($|f - f_0| \leq \frac{1}{8D}$, with 15 frequencies). Each data run is analyzed four times using the data points restricted to these four frequency ranges.

The line-shape that results from plotting $\overline{\Delta\theta}$ versus microwave frequency is very nearly described by the simple linear expression $\Delta\omega T$ (see section 2.1), an example of which is shown in figure 4.2(a). The Fr1 frequency range is used to calculate all centres shown in figures 5.1 and 5.2, except for panel (f), where each of the points represent analysis within each of the four frequency ranges.

A fit of all $\overline{\Delta\theta}$ data (to the line shape of equation 2.2) taken with $T = 300$ ns, $D = 100$ ns, and at 100% power (corresponding to V=2.03 rad/s), within the Fr1 frequency range, is shown in figure 4.2(a) and gives an f_0 determination with an uncertainty of only 13 Hz. On a 300-times expanded scale in figure 4.2(b), where the $\Delta\omega T$ straight line is subtracted, one can see that the averaged data analyzed within Fr1 is described well by the line-shape of equation 2.2. The residuals from this fit, shown in figure 4.2(e), are consistent with zero and are 100 000 times smaller than the range shown in figure 4.2(a), indicating that the line-shape is understood at this level.

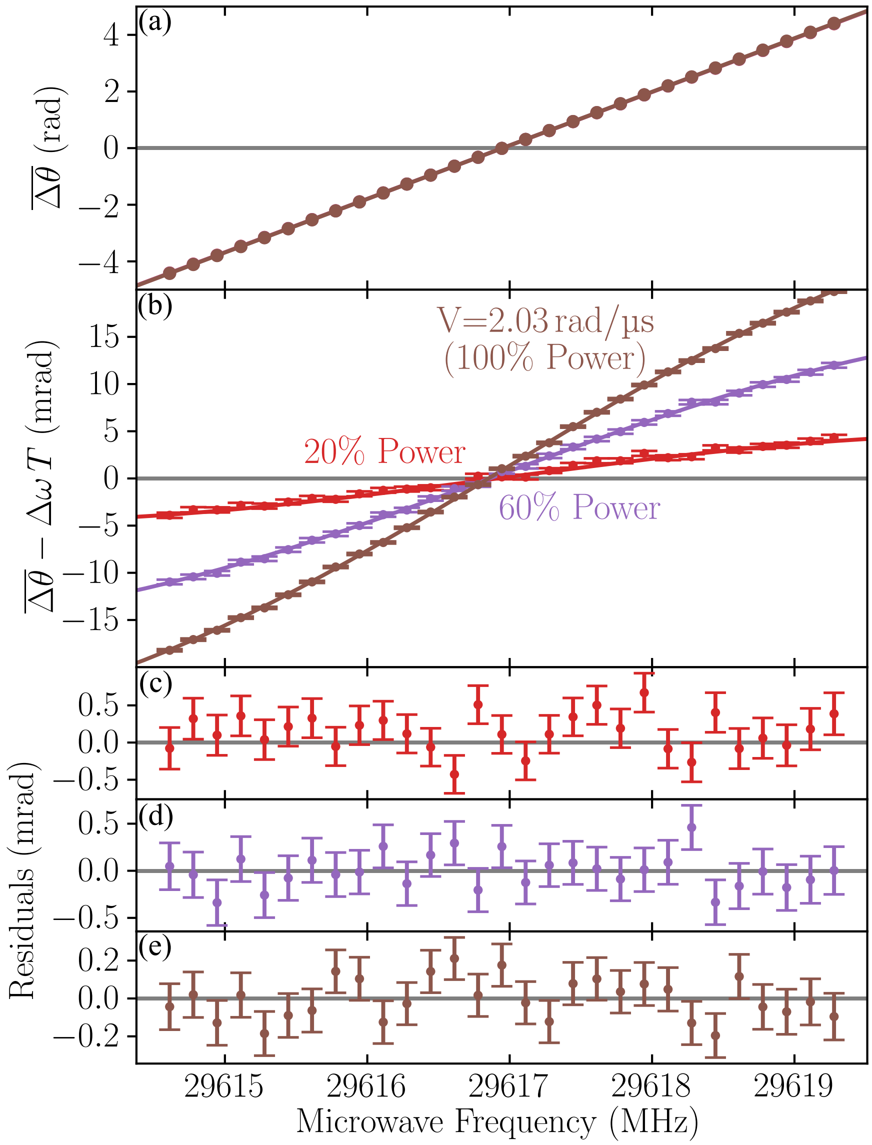

Figure 4.2: The FOSOF line-shape for data taken with $T = 300$ ns and $D = 100$ ns at 100% power (corresponding to V=2.03 rad/s). $\overline{\Delta\theta}$ =($\Delta\theta_{(\mathrm{I})}$)−$\Delta\theta_{(\mathrm{II})}$)/2 is shown in (a). A 300-times-expanded scale in (b), with $\Delta\omega T$ subtracted, shows the residual line-shapes for different powers. The fits use equation 2.2, and the residuals from the fits are shown in (c), (d), and (e).

The data in figure 4.2 are the average of many repetitions of the measurements taken at various times during the six months of data collection. Individual points are the average of 100 minutes of data. The excellent signal-to-noise ratio is despite the fact that the measurement sequence takes 450 ns, allowing only $e^{-(450\,\mathrm{ns})/(98\,\mathrm{ns})}$=1.0% of the 2^3P atoms to contribute to the signal. The improved statistics (cf. Ref. [21]) is mostly due to the 2D-MOT increasing the intensity of the metastable helium beam and the high efficiency of the Stark-ionization detector.

The measurement is performed blind (with respect to previous measurements of this interval) by adding an unknown offset (between -4 and $+4$ kHz) to all frequencies during analysis. This fixed unknown offset was implemented more than five years prior to publication, when this work began, and was revealed only after completing all of the analysis for the measurement.

5. Systematic Effects

In this chapter, the study of possible sources of systematic effects on the measurement is discussed.

5.1. Overview of Systematics Effects Studied

All experimental parameters varied for the main set of data used for the measurement are listed in table 5.1 and figure 5.1. Column 3 of table 5.1 and the points plotted in figure 5.1 are weighted averages of all centres from runs using the listed parameters. For both the table and the figure, all values are corrected for the systematic effects discussed in sections 5.2 through 5.5. Additional data runs taken to test for systematic effects are all taken with a pulse separation of 300 ns, a pulse duration of 100 ns, and at 100% microwave power. Weighted averages of centres obtained from these data runs are shown in table 5.2 and figure 5.2.

Table 5.1: Summary of the experimental parameters used for the main data runs. Column 3 lists values for $\Delta\nu_f = \nu_{\text{subset}} - \nu_{\text{final}}$, where $\nu_{\text{final}} = 29,616,955,018$ Hz is our final measured linecentre obtained from taking a weighted average of all data runs in appendix A.1 and ν_{subset} is the linecentre calculated using the subset of this data that corresponds to the specified parameter value. These centres include the systematic corrections discussed in sections 5.2 through 5.5.

Experimental Parameters	Parameter Values	$\Delta\nu_f$ [Hz]	Panel on Figure 5.1
Microwave Pulse Timings - (T, D) [ns]	(300, 50)	3(77)	(b)
	(300, 100)	-23(36)	
	(400, 100)	50(38)	
	(500, 100)	53(53)	
	(400, 200)	9(40)	
	(500, 200)	86(41)	
	(600, 200)	25(52)	
Microwave Pulse Separation - T [ns]	300	-18(34)	(c)
	400	32(29)	
	500	-38(33)	
	600	25(52)	
Microwave Pulse Duration - D [ns]	50	3(77)	(d)
	100	22(32)	
	200	-30(36)	
Magnetic Field Direction - $\hat{B}$	$-\hat{z}$	24(33)	(a)
	$+\hat{z}$	-24(32)	
Magnetic Field Magnitude - $\|\vec{B}\|$ [G]	5	-11(29)	(a)
	10	46(39)	
	15	-40(60)	
m_J of Initial 2^3S State	-1	-17(32)	(e)
	+1	20(33)	
FOSOF Offset Frequency [Hz]	280	9(32)	(g)
	-280	-11(32)	
Frequency Range Used for Linecentre Determination	$\|f - f_0\| \leq \frac{3}{4D}$ (Fr0)	-6(25)	(f)
	$\|f - f_0\| \leq \frac{1}{2D}$ (Fr1)	0(25)	
	$\|f - f_0\| \leq \frac{1}{4D}$ (Fr2)	-9(26)	
	$\|f - f_0\| \leq \frac{1}{8D}$ (Fr4)	-11(32)	

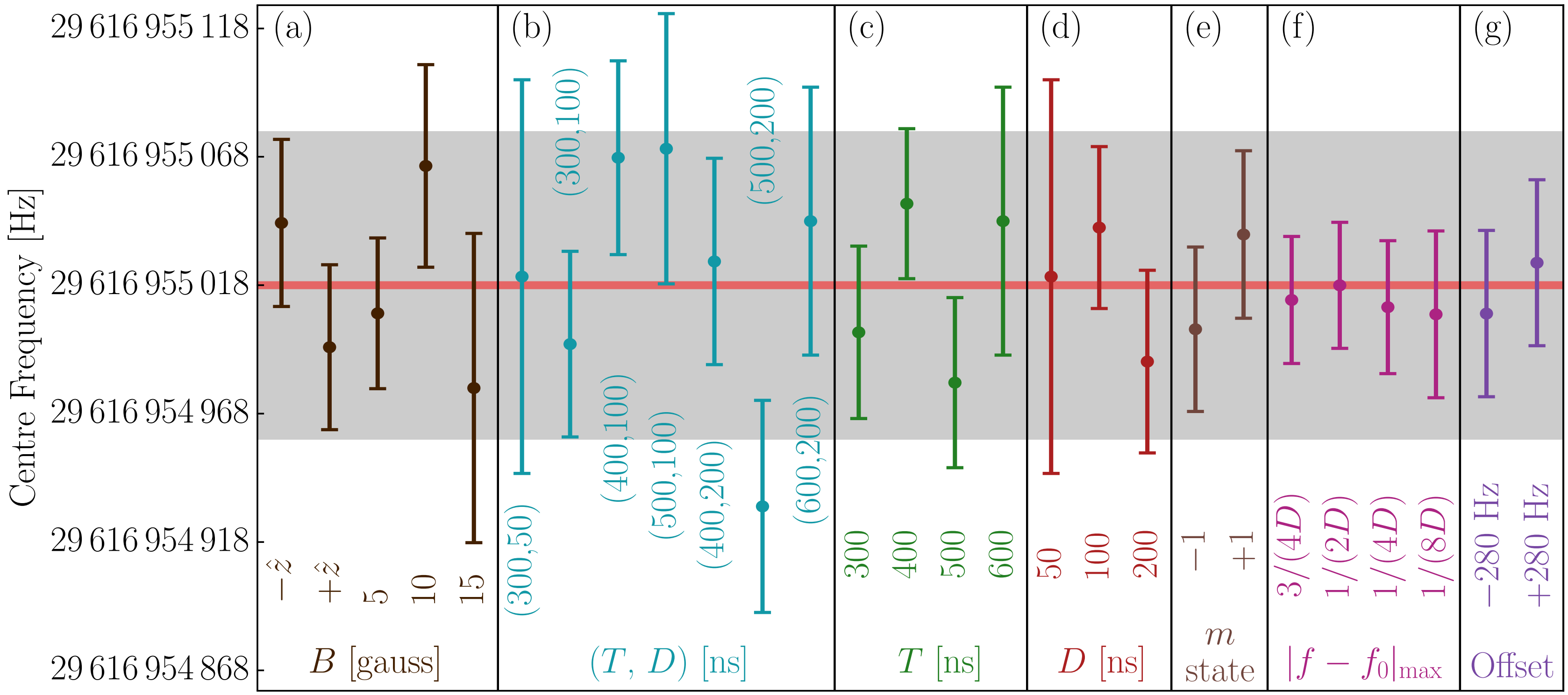

Figure 5.1: A plot of the average linecentres obtained for the various values of the experimental parameters (as listed in table 5.1). All points use the frequency range $|f - f_0| < 1/(2D)$, unless otherwise specified, and include the systematic corrections discussed in sections 5.2 through 5.5. Parts (a) through (g) show the average line centres for different B, T, D, m, $|f - f_0|$, and offset frequency, respectively. The grey band represents the final uncertainty range for the present measurement.

Table 5.2: Summary of the additional experimental parameters varied to test for systematic effects. All of this additional data is taken at 100% microwave power, with a pulse separation of T = 300 ns and a pulse duration of D = 100 ns. Column 3 lists values for $\Delta\nu_{\mathrm{s}} = \nu_{\mathrm{subset}} - \nu_{\mathrm{standard}}$. ν_{standard} is the linecentre calculated using data from appendix A.1 that is taken at 100% microwave power, with a pulse separation of T = 300 ns and a pulse duration of D = 100 ns. ν_{subset} is the linecentre obtained using data corresponding to the experimental parameter specified in column 1.

Experimental Parameters	$\Delta\nu_{\mathrm{s}}$ [Hz]	Section on Figure 5.2
25% 1083-nm Bump-up Laser Power 30% 447-nm Laser Power	9(24) 3(24)	(a)
Transition from $J = 0$ to $J = 1$ instead of $J = 1$ to $J = 0$	-21(26)	(b)
Stark Ionization and Detection on 18F instead of 18P	-27(28)	(c)
He* Source Cooled by Ice-water Bath ($T_{source} = 316$ K)	-8(17)	(d)
Linear Polarization of Bump-up Misaligned by 10 Degrees	-22(24)	(e)

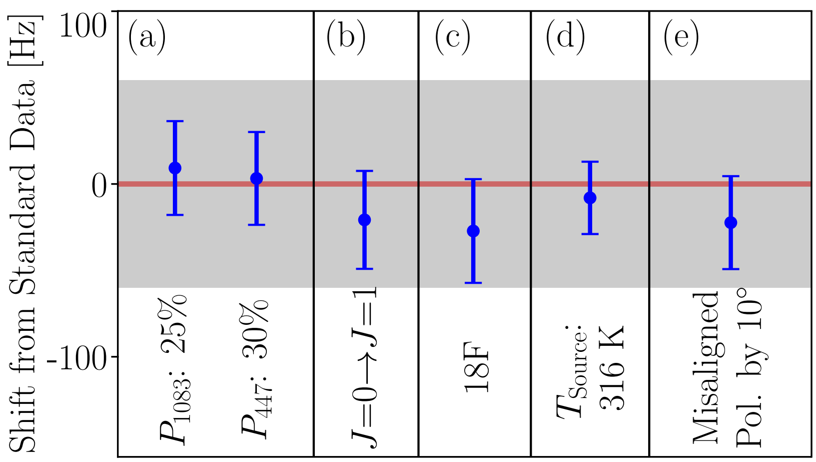

Figure 5.2: A summary of the shifts of linecentres (for T=300 ns, D=100 ns, and 100% power) obtained with non-standard parameter values (compared to similar linecentres with standard parameter values). The grey band represents the final uncertainty for the present measurement.

5.2. Magnetic Field Corrections

The microwave transition studied occurs in a DC magnetic field $|\vec{B}|$ of 5, 10, or 15 gauss generated by a pair of 20-cm-diameter Helmholtz coils that are situated inside of the experiment chamber, as shown in figure 3.2. Before applying this field, the local background magnetic field (Earth's magnetic field and stray fields in the laboratory) is cancelled using six larger coils that surround the experiment chamber. This cancellation is achieved by comparing the magnitude of the quadratic Zeeman shifts of the $2\,^3P_1$-to-$2\,^3P_0$ interval when positive and negative fields are applied.

The largest systematic correction in the measurement is the second-order (quadratic) Zeeman shift, which is 197.74 Hz/gauss^2 for the $2\,^3P_1$-to-$2\,^3P_0$ interval. This quadratic shift has been carefully studied (at the $<$0.01% level of accuracy) by theory [72], and experiment [18, 73]. Larger magnetic fields are used to directly show that the magnetic shifts are understood at a level of $<$0.1%, and a 0.1% uncertainty is included for all Zeeman corrections. The Zeeman-shift corrections $\Delta\nu_{\text{zeem}}$ and their uncertainties $\delta\nu_{\text{zeem}}$ are given in appendix A.1 for each of the 680 types of data taken. Figure 5.1(a) shows the weighted average of centres obtained with $\vec{B}$ in the $+\hat{z}$ and $-\hat{z}$ directions agree, and that those with $|\vec{B}|$=5 gauss agree with those taken for $|\vec{B}|$=10 gauss and $|\vec{B}|$=15 gauss (which have four and nine times larger Zeeman shifts, respectively).

5.3. Doppler Shift

The Doppler shift is small due to both the slow speed (1100 m/s) of our atoms (measured by the time-of-flight delay after passing through a mechanical chopper) and the fact that the microwaves travel in a direction that is perpendicular (to within 5 mrad) to the velocity of the atoms. Examples of the time-of-flight delay signals used to determine velocity for both cooling with LN2 and ice-water are shown in figure 5.3. A warmer source temperature (315 K, c.f. 130 K), and hence a faster atomic beam does not shift the linecentre, as shown in figure 5.2(d).

The Doppler shift is further reduced by reflecting the microwaves from a short and having them intersect the atomic beam a second time. Ohmic heating by the microwaves of the gold-plated waveguide is calculated to lead to a difference of only 0.4% for power of the reflected microwaves. Taking into account the slow He* beam speed, the nearly perpendicular angle of the propagation direction, and the nearly equal power of the counter-propagating microwave pulses, the net Doppler shift is 0 ± 2 Hz.

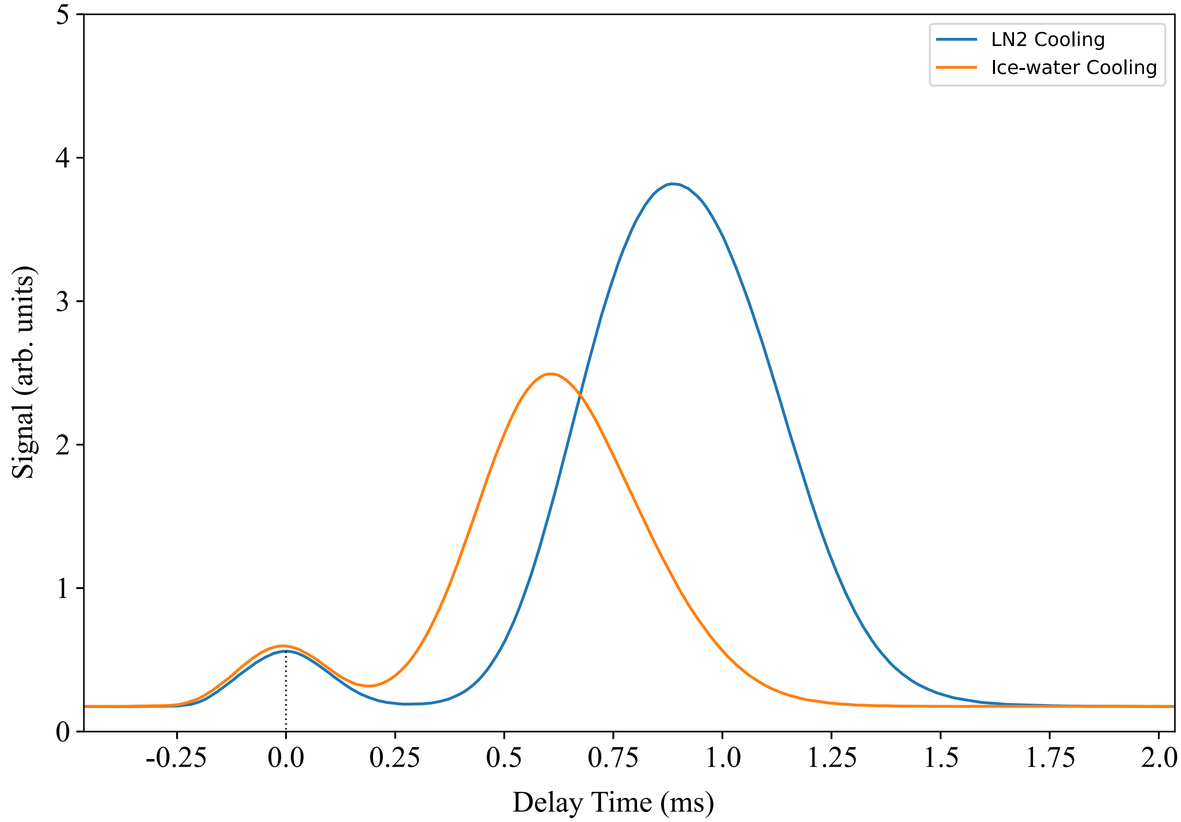

Figure 5.3: Time-of-flight measurements for the source being cooled with liquid nitrogen and with ice-water mixture. The peak at t = 0 (marked with a dotted line) is the detected photons that pass through the chopper and the right peak is the He* atoms detected (approximately 110 cm downstream of the chopper) with a delay caused by their slow velocity.

5.4. Laser and Microwave Imperfections

The polarization for optical-pumping is reversed for half of the measurements, leading to a starting population in the 2^3S $(m{=}{+}1)$ state, rather than the 2^3S $(m{=}{-}1)$ state. Figure 5.1(e) shows that consistent results are obtained with $m{=}{+}1$ and -1. To test for possible FOSOF line-shape effects, the data are refit with only the central frequencies ($|f{-}f_0|{<}1/(2D)$, $1/(4D)$, or $1/(8D)$) included in the fit. Consistent results are found, as shown in figure 5.1(f). Figure 5.1(g) shows that the result does not depend on the sign of the offset frequency.

To test for light shifts due to unintended temporal overlap of the laser and microwave pulses, data are taken at lower powers for the 447-nm and 1083-nm lasers. No shifts are seen, as shown in figure 5.2(a). The fact that the same result is obtained (figure 5.2(b)) when driving the $2\,^3$P$_1$-to-$2\,^3$P$_0$ and $2\,^3$P$_0$-to-$2\,^3$P$_1$ microwave transitions (by retuning lasers A and B of figure 3.3) and when using the 18^3F Rydberg state instead of the 18^3P Rydberg state (see figure 5.2(c)), indicates that unintended atomic processes are not affecting the measurement.

Finally, intentionally misaligning the linear polarization of laser A of figure 3.3 by 10° away from perpendicular to the applied $\vec{B}$ field leads to no change in the centre (as shown in figure 5.2(e)). This latter test (along with the test of figure 5.2(b) and the fact that the result is independent of magnetic field) shows that transitions from 2^3P$_1$$(m{=}{\pm}1)$ to 2^3P$_0$ (that would be possible if the microwave polarization were not perfect) do not have a significant effect on the measurement.

5.5. Microwave Power Extrapolation

Extensive modelling shows that imperfect microwave pulses can cause shifts in the measured linecentre, but that these shifts are proportional to P. These shifts extrapolate exactly to zero in the zero-microwave-power limit, regardless of how the microwave pulses are distorted. Therefore, data is collected at a range of powers and measured FOSOF centres (from fits to equation 2.2) are linearly extrapolated to $P=0$, as shown in figure 5.4. These extrapolations also account for very small AC Zeeman and AC Stark shifts caused by the microwaves. Both modelling and measurements show that the slopes for these extrapolations are nearly proportional to D/T.

Data runs with various combinations of T and D confirm that all sets of parameters extrapolate to a single intercept, as shown in figure 5.1(b), (c) and (d). Both in the previous measurement [25] and in this work, some data are taken with different levels of imperfections in the microwave pulses. These resulted in slopes of measured linecentres versus microwave powers that differ by a factor of approximately three, while still resulting in consistent intercepts.

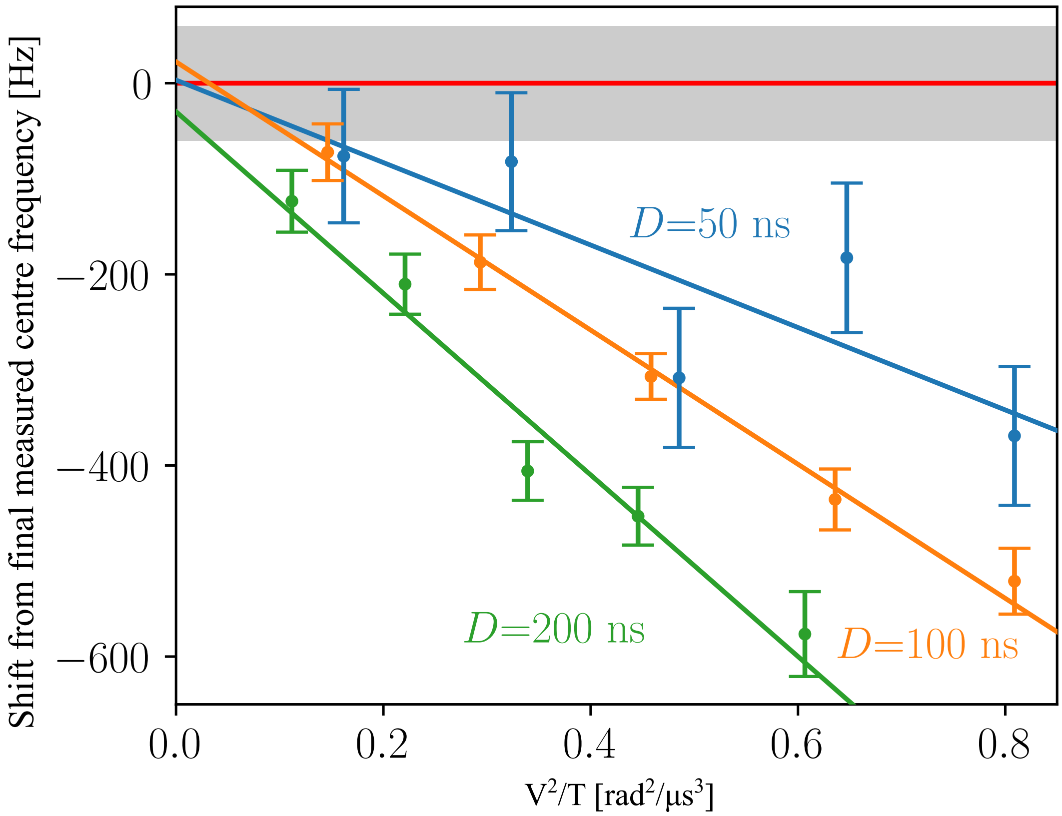

Figure 5.4: The extrapolation of the averaged D=200 ns, D=100 ns and D=50 ns FOSOF fit centres to P=0, where the centre is unaffected by imperfections in the pulses. The extrapolated centres, along with their uncertainties, are shown in figure 5.1(d). The gray band represents the final uncertainty for the present measurement.

6. Conclusion

The weighted average of the results shown in figure 5.1(b) is $29\,616\,955\,018(15)_{\mathrm{e}}(6)_{\mathrm{Z}}(2)_{\mathrm{D}}$ Hz, where the uncertainties come from the extrapolations to P=0 ($\pm$15 Hz, which is limited by statistical uncertainties), the Zeeman shift ($\pm$6 Hz), and the Doppler shift ($\pm$2 Hz). Adding the uncertainties in quadrature leads to an uncertainty of 16 Hz. However, we take a more conservative tack and base our uncertainty on the proven level of consistency demonstrated for a wide range of parameters in figure 5.1, and conservatively assign a larger estimate for our one-sigma uncertainty of $\pm$60 Hz to our measurement. This final uncertainty is one part in $30\,000$ of the natural width of the 2^3P states.

For such a precise measurement, we believe that the more conservative strategy is preferred since it tries to account for the possibility of unknown systematic effects. The possible size of such unknown effects can only be limited by looking at the level of consistency as a wide range of parameters are varied. The history of large discrepancies between precision measurements (as seen, for example, in figure 1.2) justifies taking such a conservative strategy for assigning our uncertainty. Our final measurement result is

$$[E(2^3\mathrm{P}_0) - E(2^3\mathrm{P}_1)]/h = 29\,616\,955\,018(60)\ \mathrm{Hz}. \tag{6.1}$$

Our measured value is somewhat larger (1.6 times the estimated theoretical uncertainty) than the best theoretical prediction [51], as seen in figure 6.1. As can be seen in figure 6.1, there are large disagreements with previous measurements. The measurement of Hu et al. [24] disagrees by

6.7 times their uncertainty. Our group's previous microwave measurement [21, 26] from 22 years ago also disagrees with the present measurement (by 4.5 times the uncertainty of the previous measurement). The current work agrees with the measurement of Shiner et al. [12]. With the inclusion of quantum interference corrections (and the resulting expanded uncertainties) [27, 29], it is also in reasonable agreement with the saturated-absorption measurement of Gabrielse et al. [18].

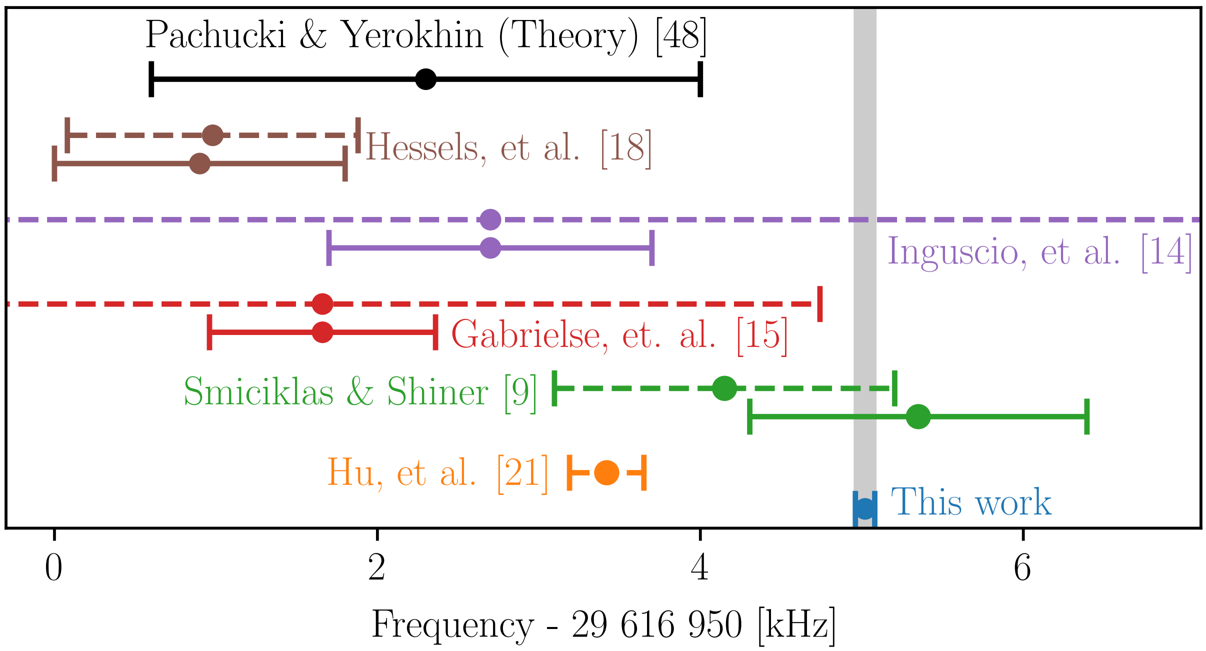

Figure 6.1: A comparison of the present measurement to previous measurements [17, 21, 23, 24] and to theory [51]. Corrected centres including quantum-interference effects [27, 29] are also shown with dashed error bars.

Although it is not our place to comment on measurements made by others, we will comment on the disagreement with our group's previous measurement. That measurement [21] was performed without the advantages of SOF or FOSOF and therefore was limited to measuring a single Lorentzian line profile without the possibility of varying timing parameters (as is done here in figure 5.1(b-d)) to search for possible systematic effects. As a result, a systematic effect (of as yet undetermined origin) must have been overlooked in that measurement. We note that if we had been as conservative then as we have chosen to be now (by expanding our 16 Hz uncertainty to 60 Hz during our blind analysis) there would have been no discrepancy between our two measurements.

Combining this measurement with our previous measurement [25] of the J=1-to-J=2 interval leads to a determination of the J=0-to-J=2 interval (which is more straightforward for theory since it does not involve the $2^3\mathrm{P}_1$ state which has a singlet-state admixture):

$$[E(2^3\mathrm{P}_0) - E(2^3\mathrm{P}_2)]/h = 31\,908\,131\,608(65)\ \mathrm{Hz}. \tag{6.2}$$

The current work is the most precise measurement to date of helium fine structure and represents a major advance in this precision. The outstanding signal-to-noise ratio has allowed for a very extensive survey of systematic effects. This work, when combined with more precise theory, could provide part-per-billion tests of the physics and constants relevant to the interval, including a precise determination of the fine-structure constant, the most precise test of QED in a multi-electron system, and tests for physics beyond the Standard Model. Further improvements in signal size (from a colder discharge source, a more efficient 2DMOT, higher microwave power, and more efficient laser excitation and detection) and a lower noise floor (from reduced collisional ionization due to a better vacuum) should allow for even smaller statistical uncertainties and more extensive tests for systematic effects.

Bibliography

[1] Richard H. Parker, Chenghui Yu, Weicheng Zhong, Brian Estey, and Holger Müller. "Measurement of the fine-structure constant as a test of the Standard Model". *Science* 360.6385 (2018), pp. 191–195.

[2] R. Bouchendira, P. Cladé, S. Guellati-Khélifa, F. Nez, and F. Biraben. "New determination of the fine structure constant and test of the quantum electrodynamics". *Phys. Rev. Lett.* 106 (2011), p. 080801.

[3] X. Fan, T. G. Myers, B. A. D. Sukra, and G. Gabrielse. "Measurement of the Electron Magnetic Moment". *Phys. Rev. Lett.* 130 (7 2023), p. 071801.

[4] Charles Schwartz. "Fine Structure of Helium". *Phys. Rev.* 134 (5A 1964), A1181–A1187.

[5] F. M. J. Pichanick, R. D. Swift, C. E. Johnson, and V. W. Hughes. "Experiments on the 2^3P State of Helium. I. A Measurement of the $2^3P_1 - 2^3P_2$ Fine Structure". *Phys. Rev.* 169 (1 1968), pp. 55–78.

[6] A. Kponou, V. W. Hughes, C. E. Johnson, S. A. Lewis, and F. M. J. Pichanick. "Precise Measurement of the $2^3P_0 - 2^3P_1$ Fine-Structure Interval of Helium". *Phys. Rev. Lett.* 26 (26 1971), pp. 1613–1616.

[7] A. Kponou, V. W. Hughes, C. E. Johnson, S. A. Lewis, and F. M. J. Pichanick. "Experiments on the 2^3P state of helium. III. Measurement of the $2^3P_0 - 2^3P_1$ fine-structure interval". *Phys. Rev. A* 24 (1 1981), pp. 264–278.

[8] W. Frieze, E. A. Hinds, V. W. Hughes, and F. M. J. Pichanick. “Experiments on the 2^3P state of helium. IV. Measurement of the $2^3P_0 - 2^3P_2$ fine-structure interval”. *Phys. Rev. A* 24 (1 1981), pp. 279–287.

[9] D. Shiner, R. Dixson, and P. Zhao. “Precise measurement of the Lamb shift and fine structure of the 2S-2P transition in triplet helium”. *Phys. Rev. Lett.* 72 (12 1994), pp. 1802–1805.

[10] D L Shiner and R Dixson. “Measuring the fine structure constant using helium fine structure”. *IEEE Trans. Instr. Meas.* 44.2 (1995), pp. 518–521.

[11] J. Castillega, D. Livingston, A. Sanders, and D. Shiner. “Precise Measurement of the $J = 1$ to $J = 2$ Fine Structure Interval in the $2P3$ State of Helium”. *Phys. Rev. Lett.* 84.19 (2000), pp. 4321–4324.

[12] Marc Smiciklas and David Shiner. “Determination of the Fine Structure Constant Using Helium Fine Structure”. *Phys. Rev. Lett.* 105.12 (2010), p. 123001.

[13] M Prevedelli, P Cancio, G Giusfredi, F S Pavone, and M Inguscio. “Frequency control of DBR diode lasers at 1.08 micrometer and precision spectroscopy of helium”. *Opt. Comm.* 125.4-6 (1996), pp. 231–236.

[14] F. Minardi, G. Bianchini, P. C. Pastor, G. Giusfredi, F. S. Pavone, and M. Inguscio. “Measurement of the Helium $2^3P_0 - 2^3P_1$ Fine Structure Interval”. *Phys. Rev. Lett.* 82 (6 1999), pp. 1112–1115.

[15] P. C. Pastor, G. Giusfredi, P. De Natale, G. Hagel, C. de Mauro, and M. Inguscio. “Absolute Frequency Measurements of the $23S1 \rightarrow 23P, 1, 2$ Atomic Helium Transitions around 1083 nm”. *Phys. Rev. Lett.* 92.2 (2004), p. 023001.

[16] P. C. Pastor, G. Giusfredi, P. De Natale, G. Hagel, C. de Mauro, and M. Inguscio. “Erratum: Absolute Frequency Measurements of the $2^3S_1 \rightarrow 2^3P_{0,1,2}$ Atomic Helium Transitions around 1083 nm [Phys. Rev. Lett. 92, 023001 (2004)]”. *Phys. Rev. Lett.* 97 (13 2006), p. 139903.

[17] G Giusfredi, P Cancio Pastor, P De Natale, D Mazzotti, C de Mauro, L Fallani, G Hagel, V Krachmalnicoff, and M Inguscio. “Present status of the fine-structure frequencies of the 23P helium level”. *Can. J. Phys.* 83.4 (2005), pp. 301–310.

[18] T. Zelevinsky, D. Farkas, and G. Gabrielse. “Precision Measurement of the Three $23PJ$ Helium Fine Structure Intervals”. *Phys. Rev. Lett.* 95.20 (2005), p. 203001.

[19] C. H. Storry and E. A. Hessels. “Precision microwave measurement of the $2^3P_1 - 2^3P_0$ interval in atomic helium”. *Phys. Rev. A* 58 (1 1998), R8–R11.

[20] C. H. Storry, M. C. George, and E. A. Hessels. “Precision Microwave Measurement of the $23P1 - 23P2$ Interval in Atomic Helium”. *Phys. Rev. Lett.* 84.15 (2000), pp. 3274–3277.

[21] M. C. George, L. D. Lombardi, and E. A. Hessels. “Precision Microwave Measurement of the $23P1 - 23P$ Interval in Atomic Helium: A Determination of the Fine-Structure Constant”. *Phys. Rev. Lett.* 87.17 (2001), p. 173002.

[22] J. S. Borbely, M. C. George, L. D. Lombardi, M. Weel, D. W. Fitzakerley, and E. A. Hessels. “Separated oscillatory-field microwave measurement of the $2P31 - -2P32$ fine-structure interval of atomic helium”. *Phys. Rev. A* 79.6 (2009), p. 060503.

[23] G.-P. Feng, X. Zheng, Y. R. Sun, and S.-M. Hu. *Phys. Rev. A* 91 (2015), p. 030502.

[24] X. Zheng, Y. R. Sun, J.-J. Chen, W. Jiang, K. Pachucki, and S.-M. Hu. *Phys. Rev. Lett.* 118 (2017), p. 063001.

[25] K. Kato, T. D. G. Skinner, and E. A. Hessels. "Ultrahigh-Precision Measurement of the $n = 2$ Triplet P Fine Structure of Atomic Helium Using Frequency-Offset Separated Oscillatory Fields". *Phys. Rev. Lett.* 121 (14 2018), p. 143002.

[26] A. Marsman, M. Horbatsch, and E. A. Hessels. "Shifts due to neighboring resonances for microwave measurements of the 2^3P fine-structure of helium". *Phys. Rev. A* 86 (2012), p. 012510.

[27] A. Marsman, M. Horbatsch, and E. A. Hessels. "Shifts due to distant neighboring resonances for laser measurements of $2^3S_1 - to - 2^3P_J$ transitions of helium". *Phys. Rev. A* 86 (2012), p. 040501.

[28] A. Marsman, E. A. Hessels, and M. Horbatsch. "Shifts due to quantum-mechanical interference from distant neighboring resonances for saturated fluorescence spectroscopy of the $2^3S - to - 2^3P$ intervals of helium". *Phys. Rev. A* 89 (2014), p. 043403.

[29] A. Marsman, M. Horbatsch, and E. A. Hessels. "Quantum interference effects in saturated absorption spectroscopy of n= 2 triplet-helium fine structure". *Phys. Rev. A* 91 (2015), p. 062506.

[30] A. Marsman, M. Horbatsch, and E. A. Hessels. "The effect of quantum-mechanical interference on precise measurements of the n= 2 triplet P fine structure of helium". *J. Phys. and Chem. Ref. Data* 44 (2015), p. 031207.

[31] B. Schiff, C. L. Pekeris, and H. Lifson. "Fine Structure of the 2^3P and 3^3P States of Helium". *Phys. Rev.* 137 (6A 1965), A1672–A1675.

[32] Kee Yong Kim. “Relativistic Corrections to the Fine Structure of Helium”. *Phys. Rev.* 140 (5A 1965), A1498–A1504.

[33] Lars Hambro. “Second-Order Corrections to the Fine Structure of Helium”. *Phys. Rev. A* 5 (5 1972), pp. 2027–2045.

[34] Lars Hambro. “Second-Order Corrections to the Fine Structure of Helium. II. Contributions from ^1P and ^3D Intermediate States”. *Phys. Rev. A* 6 (3 1972), pp. 865–870.

[35] Lars Hambro. “Second-Order Corrections to the Fine Structure of Helium. III. Improved Calculation of Some ^3P Contributions”. *Phys. Rev. A* 7 (2 1973), pp. 479–486.

[36] Marvin Douglas and Norman M Kroll. “Quantum electrodynamics corrections to the fine structure of helium”. *Ann. Phys. (N.Y.)* 82.1 (1974), pp. 89–155.

[37] James Daley, Marvin Douglas, Lars Hambro, and Norman M. Kroll. “New Theoretical Values of the 2^3P Fine-Structure Splittings of Helium”. *Phys. Rev. Lett.* 29 (1 1972), pp. 12–15.

[38] Michael L. Lewis and Paul H. Serafino. “Second-order contributions to the fine structure of helium from all intermediate states”. *Phys. Rev. A* 18 (3 1978), pp. 867–888.

[39] Zong-Chao Yan and G. W. F. Drake. “High Precision Calculation of Fine Structure Splittings in Helium and He-Like Ions”. *Phys. Rev. Lett.* 74 (24 1995), pp. 4791–4794.

[40] Tao Zhang. “Corrections to $O(\alpha^7 ln\alpha)mc^2$) fine-structure splittings and $O(\alpha^6 ln\alpha mc^2)$ energy levels in helium”. *Phys. Rev. A* 54 (2 1996), pp. 1252–1312.

[41] Tao Zhang. “QED corrections to $\alpha^7 mc^2$ fine-structure splittings in helium”. *Phys. Rev. A* 53 (6 1996), pp. 3896–3914.

[42] Tao Zhang, Zong-Chao Yan, and G. W. F. Drake. "QED Corrections of $O(mc^2\alpha^7 ln\alpha)$ to the Fine Structure Splittings of Helium and He-like Ions". *Phys. Rev. Lett.* 77 (9 1996), pp. 1715–1718.

[43] G. W. F. Drake. "Progress in helium fine-structure calculations and the fine-structure constant". *Can. J. Phys.* 80.11 (2002), pp. 1195–1212.

[44] Krzysztof Pachucki and Jonathan Sapirstein. "Contributions to helium fine structure of order mα^7". *J. Phys. B* 33.23 (2000), p. 5297.

[45] Krzysztof Pachucki and Jonathan Sapirstein. "Higher-order recoil corrections to helium fine structure". *J. Phys. B* 36.5 (2003), p. 803.

[46] J Sapirstein. "Momentum space P-state helium wavefunctions and helium fine structure". *J. Phys. B* 43.7 (2010), p. 074015.

[47] Krzysztof Pachucki. "Quantum electrodynamics effects on helium fine structure". *J. Phys. B* 32.1 (1999), p. 137.

[48] Krzysztof Pachucki. "Improved Theory of Helium Fine Structure". *Phys. Rev. Lett.* 97 (1 2006), p. 013002.

[49] Krzysztof Pachucki and Vladimir A. Yerokhin. "Reexamination of the helium fine structure". *Phys. Rev. A* 79 (6 2009), p. 062516.

[50] Krzysztof Pachucki and Vladimir A. Yerokhin. "Publisher's Note: Reexamination of the helium fine structure [Phys. Rev. A 79, 062516 (2009)]". *Phys. Rev. A* 80 (1 2009), p. 019902.

[51] Krzysztof Pachucki and Vladimir A. Yerokhin. "Fine Structure of Heliumlike Ions and Determination of the Fine Structure Constant". *Phys. Rev. Lett.* 104 (7 2010), p. 070403.

[52] Krzysztof Pachucki and Vladimir A. Yerokhin. “FINE STRUCTURE OF HELIUM AND HELIUM-LIKE IONS”. *Can. J. Phys.* 89 (2011), p. 95.

[53] Zhang Pei-Pei, Zhong Zhen-Xiang, Yan Zong-Chao, and Shi Ting-Yun. “Precision calculation of fine structure in helium and Li+”. *Chinese Physics B* 24.3 (2015), p. 033101.

[54] JR Lifsitz. “A measurement of the triplet-2p fine structure of helium-4”. PhD thesis. University of Michigan Thesis, 1965.

[55] Farshad Heydarizadmotlagh, TDG Skinner, Kosuke Kato, MC George, and EA Hessels. “Precision Measurement of the n= 2 Triplet PJ= 1 to J= 0 Fine Structure of Atomic Helium Using Frequency-Offset Separated Oscillatory Fields”. *Physical Review Letters* 132.16 (2024), p. 163001.

[56] K. Pachucki, V. Patkóš, and V. A. Yerokhin. “Testing fundamental interactions on the helium atom”. *Phys. Rev. A* 95 (2017), p. 062510.

[57] F. Ficek, D. F. Jackson, M. G. Kozlov, N. Leefer, S. Pustelny, and D. Budker. “Constraints on exotic spin-dependent interactions between electrons from helium fine-structure spectroscopy”. *Phys. Rev. A* 95 (2017), p. 032505.

[58] T. Aoyama, M. Hayakawa, T. Kinoshita, and M. Nio. “Tenth-order QED contribution to the electron g- 2 and an improved value of the fine structure constant”. *Phys. Rev. Lett.* 109 (2012), p. 111807.

[59] S. Laporta. “High-precision calculation of the 4-loop contribution to the electron g-2 in QED”. *Phys. Lett. B* 772 (2017), p. 232.

[60] T. Aoyama, T. Kinoshita, and M. Nio. "Revised and improved value of the QED tenth-order electron anomalous magnetic moment". *Phys. Rev. D* 97 (2018), p. 036001.

[61] Sergey Volkov. "Calculating the five-loop QED contribution to the electron anomalous magnetic moment: Graphs without lepton loops". *Phys. Rev. D* 100 (9 2019), p. 096004.

[62] G Gabrielse, S Fogwell Hoogerheide, J Dorr, and E Novitski. "Precise Matter and Antimatter Tests of the Standard Model with e-, e+, p, $\overline{\mathrm{P}}$ and $\overline{\mathrm{H}}$". In: *Fundamental Physics in Particle Traps*. Springer, 2014, pp. 1–40.

[63] Y. Kahn, G. Krnjaic, S. Mishra-Sharma, and T. M. P. Tait. "Light weakly coupled axial forces: models, constraints, and projections". *J. High Energy Phys.* 2017.5 (2017), p. 2.

[64] Céline Bœhm and J Silk. "A new test for dark matter particles of low mass". *Physics Letters B* 661 (2008), p. 287.

[65] A. C. Vutha and E. A. Hessels. "Frequency-offset separated oscillatory fields". *Phys. Rev. A* 92 (2015), p. 052504.

[66] N. F. Ramsey. "A new molecular beam resonance method". *Phys. Rev.* 76 (1949), p. 996.

[67] N. Bezginov, T. Valdez, M. Horbatsch, A. Marsman, A.C. Vutha, and E.A. Hessels. "A measurement of the atomic hydrogen Lamb shift and the proton charge radius". *Science* 365.6457 (2019), pp. 1007–1012.

[68] Taylor David Grant Skinner. "Progress Towards a Precision Measurement of the $2^3\mathrm{P}_1$-to-$2^3\mathrm{P}_0$ Transition in Atomic Helium". PhD thesis. York University, 2024.

[69] Kosuke Kato. "Precision Microwave Frequency-Offset Separated-Oscillatory-Fields Measurement of the 2^3P_1-to-2^3P_2 Fine-Structure Interval in Atomic Helium". PhD thesis. York University, 2019.

[70] Franzen, A. (n.d.). Component Library [Vector graphics library for creating diagrams and illustrations of optics experiments]. GW Optics. Retrieved from https://www.gwoptics.org/-ComponentLibrary/.

[71] Kristan L Corwin, Zheng-Tian Lu, Carter F Hand, Ryan J Epstein, and Carl E Wieman. "Frequency-stabilized diode laser with the Zeeman shift in an atomic vapor". *Applied optics* 37.15 (1998), pp. 3295–3298.

[72] Z.-C. Yan and G. W. F. Drake. "High-precision calculations of the Zeeman effect in the 2^3P_J, 2^1P_1, 2^3S_1, and 3^3P_J states of helium". *Phys. Rev. A* 50 (1994), R1980.

[73] S. A. Lewis, F. M. J. Pichanick, and V. W. Hughes. "Experiments on the 2^3P State of Helium. II. Measurements of the Zeeman Effect". *Phys. Rev. A* 2 (1970), p. 86.

A. Appendix

A.1. Table of Condensed Experimental Data

The table A.1 includes the condensed set of all data collected and used to determine the reported linecentre. This data is analyzed using the Fr1 frequency range ($|f - f_0| \leq \frac{1}{2D}$). Each row represents the weighted average of centres and systematic corrections for runs with a unique combination of variables, which are pulse separation (T), pulse duration (D), experiment magnetic field (B), starting m state, FOSOF offset frequency, and microwave power (P). Weighted averages of the data in table A.1 is used to find the values in table 5.1 and figure 5.1.

The acronyms used in the column headers are as follows: T:Pulse separation, D: pulse duration, B: magnetic field, m-state: starting $2\,^3\mathrm{S}_1$ m state ($m = +1$ or $m = -1$), $\mathrm{f}_{\mathrm{offset}}$: FOSOF offset frequency, P: microwave power as a percentage of the maximum power used in the experiment, $\Delta\nu_{\mathrm{centre}}$: frequency offset of the data subset's linecentre (including corrections for all systematic effects) from the final linecentre reported in this work, $\delta\nu_{\mathrm{centre}}$: uncertainty in the data subset's linecentre (this uncertainty includes the uncertainties due to systematic effects), $\delta\nu_{\mathrm{stat}}$: statistical uncertainty, $\Delta\nu_{\mathrm{slope}}$: power slope correction, $\delta\nu_{\mathrm{slope}}$: power slope correction uncertainty, $\Delta\nu_{\mathrm{zeem}}$: DC Zeeman correction, $\delta\nu_{\mathrm{zeem}}$: DC Zeeman correction uncertainty, $\mathrm{T}_{\mathrm{total}}$: total measurement time used for the data subset.

Table A.1: Table of condensed experimental data.

T [ns]	D [ns]	B [G]	m-state	f_{offset} [Hz]	P [%]	$\Delta\nu_{centre}$ [Hz]	$\delta\nu_{centre}$ [Hz]	$\delta\nu_{stat}$ [Hz]	$\Delta\nu_{slope}$ [Hz]	$\delta\nu_{slope}$ [Hz]	$\Delta\nu_{zeem}$ [kHz]	$\delta\nu_{zeem}$	T_{total} [Mins]
300	50	-15	-1	-280	20	340	314	310	-58	21	45	45	314
300	50	-15	-1	280	20	178	307	303	-58	21	45	45	310
300	50	-15	1	-280	20	-814	328	324	-58	21	45	45	629
300	50	-15	1	280	20	909	417	414	-58	21	45	45	592
300	50	-15	-1	-280	40	-11	257	250	-117	42	45	45	126
300	50	-15	-1	280	40	14	255	248	-117	42	45	45	133
300	50	-15	1	-280	40	-151	425	420	-117	42	45	45	102
300	50	-15	1	280	40	565	591	588	-117	42	45	45	85
300	50	-15	-1	-280	60	-293	296	286	-175	63	45	45	69
300	50	-15	-1	280	60	37	274	263	-175	63	45	45	69
300	50	-15	1	-280	60	-600	541	536	-175	63	45	45	40
300	50	-15	1	280	60	-445	523	517	-175	63	45	45	39
300	50	-15	-1	-280	80	113	300	284	-233	85	45	45	51
300	50	-15	-1	280	80	61	301	286	-233	85	45	45	50
300	50	-15	1	-280	80	700	607	600	-233	85	45	45	19
300	50	-15	1	280	80	976	522	513	-233	85	45	45	22
300	50	-15	-1	-280	100	28	327	306	-292	106	45	45	32
300	50	-15	-1	280	100	315	350	331	-292	106	45	45	32
300	50	-15	1	-280	100	-918	465	451	-292	106	45	45	24
300	50	-15	1	280	100	-411	509	496	-292	106	45	45	21
300	50	-10	-1	-280	20	-344	273	272	-58	21	20	20	279
300	50	-10	-1	280	20	130	289	287	-58	21	20	20	245
300	50	-10	1	-280	20	386	331	330	-58	21	20	20	580
300	50	-10	1	280	20	-666	307	305	-58	21	20	20	605
300	50	-10	-1	-280	40	-95	286	282	-117	42	20	20	109
300	50	-10	-1	280	40	226	281	277	-117	42	20	20	115
300	50	-10	1	-280	40	646	451	448	-117	42	20	20	97
300	50	-10	1	280	40	-549	397	394	-117	42	20	20	94
300	50	-10	-1	-280	60	136	273	264	-175	63	20	20	60
300	50	-10	-1	280	60	-372	290	282	-175	63	20	20	56

T [ns]	D [ns]	B [G]	m-state	f_{offset} [Hz]	P [%]	ν_{centre} [Hz]	$\delta\nu_{centre}$ [Hz]	$\delta\nu_{stat}$ [Hz]	$\Delta\nu_{slope}$ [Hz]	$\Delta\nu_{slope}$ [Hz]	$\Delta\nu_{zeem}$ [kHz]	$\delta\nu_{zeem}$	T_{total} [Mins]
300	50	-10	1	-280	60	-260	470	466	-175	63	20	20	35
300	50	-10	1	280	60	-100	447	442	-175	63	20	20	41
300	50	-10	-1	-280	80	660	281	267	-233	85	20	20	43
300	50	-10	-1	280	80	57	266	251	-233	85	20	20	43
300	50	-10	1	-280	80	407	428	419	-233	85	20	20	23
300	50	-10	1	280	80	133	414	404	-233	85	20	20	27
300	50	-10	-1	-280	100	338	322	303	-292	106	20	20	28
300	50	-10	-1	280	100	-88	297	277	-292	106	20	20	28
300	50	-10	1	-280	100	-243	419	405	-292	106	20	20	21
300	50	-10	1	280	100	477	416	402	-292	106	20	20	22
300	50	-5	-1	-280	20	135	328	327	-58	21	5	5	226
300	50	-5	-1	280	20	80	305	304	-58	21	5	5	230
300	50	-5	1	-280	20	-44	286	285	-58	21	5	5	666
300	50	-5	1	280	20	98	365	365	-58	21	5	5	540
300	50	-5	-1	-280	40	438	293	290	-117	42	5	5	94
300	50	-5	-1	280	40	-92	265	262	-117	42	5	5	111
300	50	-5	1	-280	40	1099	355	353	-117	42	5	5	122
300	50	-5	1	280	40	-194	343	340	-117	42	5	5	110
300	50	-5	-1	-280	60	108	298	292	-175	63	5	5	54
300	50	-5	-1	280	60	-3	286	279	-175	63	5	5	56
300	50	-5	1	-280	60	-343	384	379	-175	63	5	5	43
300	50	-5	1	280	60	-115	355	349	-175	63	5	5	52
300	50	-5	-1	-280	80	-42	261	247	-233	85	5	5	45
300	50	-5	-1	280	80	-31	269	256	-233	85	5	5	45
300	50	-5	1	-280	80	-390	488	480	-233	85	5	5	23
300	50	-5	1	280	80	131	402	393	-233	85	5	5	22
300	50	-5	-1	-280	100	-313	330	313	-292	106	5	5	28
300	50	-5	-1	280	100	-391	318	300	-292	106	5	5	28
300	50	-5	1	-280	100	105	360	344	-292	106	5	5	21
300	50	-5	1	280	100	-51	377	361	-292	106	5	5	28
300	50	5	-1	-280	20	-589	330	329	-58	21	5	5	604
300	50	5	-1	280	20	106	373	372	-58	21	5	5	564

T [ns]	D [ns]	B [G]	m-state	f_{offset} [Hz]	P [%]	ν_{centre} [Hz]	$\delta\nu_{centre}$ [Hz]	$\delta\nu_{stat}$ [Hz]	$\Delta\nu_{slope}$ [Hz]	$\Delta\nu_{slope}$ [Hz]	$\Delta\nu_{zeem}$ [kHz]	$\delta\nu_{zeem}$	T_{total} [Mins]
300	50	5	1	-280	20	176	345	344	-58	21	5	5	222
300	50	5	1	280	20	309	321	320	-58	21	5	5	235
300	50	5	-1	-280	40	87	417	414	-117	42	5	5	103
300	50	5	-1	280	40	-521	360	357	-117	42	5	5	118
300	50	5	1	-280	40	-117	331	329	-117	42	5	5	99
300	50	5	1	280	40	57	275	272	-117	42	5	5	92
300	50	5	-1	-280	60	-211	383	378	-175	63	5	5	43
300	50	5	-1	280	60	-219	368	363	-175	63	5	5	45
300	50	5	1	-280	60	-11	291	284	-175	63	5	5	56
300	50	5	1	280	60	-25	307	300	-175	63	5	5	53
300	50	5	-1	-280	80	-403	422	414	-233	85	5	5	22
300	50	5	-1	280	80	33	461	454	-233	85	5	5	27
300	50	5	1	-280	80	314	304	292	-233	85	5	5	42
300	50	5	1	280	80	106	314	302	-233	85	5	5	45
300	50	5	-1	-280	100	57	352	336	-292	106	5	5	22
300	50	5	-1	280	100	-255	393	378	-292	106	5	5	21
300	50	5	1	-280	100	-363	345	328	-292	106	5	5	28
300	50	5	1	280	100	-302	334	317	-292	106	5	5	28
300	50	10	-1	-280	20	45	360	359	-58	21	20	20	598
300	50	10	-1	280	20	-71	265	263	-58	21	20	20	643
300	50	10	1	-280	20	-100	379	378	-58	21	20	20	198
300	50	10	1	280	20	-605	365	364	-58	21	20	20	209
300	50	10	-1	-280	40	-305	317	313	-117	42	20	20	108
300	50	10	-1	280	40	-74	337	334	-117	42	20	20	109
300	50	10	1	-280	40	-181	327	323	-117	42	20	20	93
300	50	10	1	280	40	192	339	336	-117	42	20	20	95
300	50	10	-1	-280	60	-179	335	328	-175	63	20	20	45
300	50	10	-1	280	60	-522	397	392	-175	63	20	20	54
300	50	10	1	-280	60	161	302	294	-175	63	20	20	55
300	50	10	1	280	60	-715	304	296	-175	63	20	20	55
300	50	10	-1	-280	80	-87	441	432	-233	85	20	20	23
300	50	10	-1	280	80	-449	406	397	-233	85	20	20	26

T [ns]	D [ns]	B [G]	m-state	f_{offset} [Hz]	P [%]	ν_{centre} [Hz]	$\delta\nu_{centre}$ [Hz]	$\delta\nu_{stat}$ [Hz]	$\Delta\nu_{slope}$ [Hz]	$\Delta\nu_{slope}$ [Hz]	$\Delta\nu_{zeem}$ [kHz]	$\delta\nu_{zeem}$	T_{total} [Mins]
300	50	10	1	-280	80	-236	332	321	-233	85	20	20	42
300	50	10	1	280	80	-533	366	356	-233	85	20	20	41
300	50	10	-1	-280	100	304	373	357	-292	106	20	20	22
300	50	10	-1	280	100	-188	339	321	-292	106	20	20	28
300	50	10	1	-280	100	-312	345	327	-292	106	20	20	28
300	50	10	1	280	100	441	369	353	-292	106	20	20	28
300	50	15	-1	-280	20	26	289	285	-58	21	45	45	929
300	50	15	-1	280	20	425	354	351	-58	21	45	45	935
300	50	15	1	-280	20	-503	323	319	-58	21	45	45	280
300	50	15	1	280	20	257	351	347	-58	21	45	45	279
300	50	15	-1	-280	40	387	388	383	-117	42	45	45	145
300	50	15	-1	280	40	-224	362	357	-117	42	45	45	150
300	50	15	1	-280	40	-145	307	301	-117	42	45	45	130
300	50	15	1	280	40	-463	309	303	-117	42	45	45	132
300	50	15	-1	-280	60	347	370	361	-175	63	45	45	63
300	50	15	-1	280	60	272	340	331	-175	63	45	45	67
300	50	15	1	-280	60	219	299	288	-175	63	45	45	86
300	50	15	1	280	60	205	252	240	-175	63	45	45	94
300	50	15	-1	-280	80	54	376	363	-233	85	45	45	31
300	50	15	-1	280	80	1089	456	446	-233	85	45	45	30
300	50	15	1	-280	80	-185	300	284	-233	85	45	45	62
300	50	15	1	280	80	-179	318	303	-233	85	45	45	58
300	50	15	-1	-280	100	215	321	299	-292	106	45	45	33
300	50	15	-1	280	100	-62	410	394	-292	106	45	45	31
300	50	15	1	-280	100	143	306	284	-292	106	45	45	46
300	50	15	1	280	100	-317	303	281	-292	106	45	45	46
300	100	-15	-1	-280	20	93	193	187	-117	9	45	45	110
300	100	-15	-1	280	20	-31	196	190	-117	9	45	45	103
300	100	-15	1	-280	20	25	234	230	-117	9	45	45	142
300	100	-15	1	280	20	368	232	227	-117	9	45	45	142
300	100	-15	-1	-280	40	47	205	199	-235	17	45	45	60
300	100	-15	-1	280	40	287	200	194	-235	17	45	45	57

T [ns]	D [ns]	B [G]	m-state	f_{offset} [Hz]	P [%]	ν_{centre} [Hz]	$\delta\nu_{centre}$ [Hz]	$\delta\nu_{stat}$ [Hz]	$\Delta\nu_{slope}$ [Hz]	$\Delta\nu_{slope}$ [Hz]	$\Delta\nu_{zeem}$ [kHz]	$\delta\nu_{zeem}$	T_{total} [Mins]
300	100	-15	1	-280	40	-67	225	220	-235	17	45	45	78
300	100	-15	1	280	40	-196	232	227	-235	17	45	45	78
300	100	-15	-1	-280	60	-43	164	156	-352	26	45	45	50
300	100	-15	-1	280	60	-98	166	158	-352	26	45	45	53
300	100	-15	1	-280	60	24	198	192	-352	26	45	45	71
300	100	-15	1	280	60	-283	197	190	-352	26	45	45	71
300	100	-15	-1	-280	80	-95	198	190	-470	34	45	45	32
300	100	-15	-1	280	80	234	213	205	-470	34	45	45	28
300	100	-15	1	-280	80	1	227	220	-470	34	45	45	39
300	100	-15	1	280	80	-203	230	223	-470	34	45	45	39
300	100	-15	-1	-280	100	116	184	174	-587	43	45	45	32
300	100	-15	-1	280	100	148	184	173	-587	43	45	45	28
300	100	-15	1	-280	100	-186	232	224	-587	43	45	45	39
300	100	-15	1	280	100	-249	228	219	-587	43	45	45	39
300	100	-10	-1	-280	20	190	143	141	-117	9	20	20	170
300	100	-10	-1	280	20	130	145	143	-117	9	20	20	156
300	100	-10	1	-280	20	-41	162	160	-117	9	20	20	172
300	100	-10	1	280	20	240	171	169	-117	9	20	20	171
300	100	-10	-1	-280	40	189	142	139	-235	17	20	20	89
300	100	-10	-1	280	40	15	148	146	-235	17	20	20	89
300	100	-10	1	-280	40	169	165	163	-235	17	20	20	92
300	100	-10	1	280	40	8	167	165	-235	17	20	20	92
300	100	-10	-1	-280	60	25	135	131	-352	26	20	20	78
300	100	-10	-1	280	60	178	135	131	-352	26	20	20	78
300	100	-10	1	-280	60	-158	147	144	-352	26	20	20	90
300	100	-10	1	280	60	76	141	137	-352	26	20	20	85
300	100	-10	-1	-280	80	269	166	162	-470	34	20	20	42
300	100	-10	-1	280	80	99	157	152	-470	34	20	20	46
300	100	-10	1	-280	80	-26	170	165	-470	34	20	20	46
300	100	-10	1	280	80	-24	182	177	-470	34	20	20	46
300	100	-10	-1	-280	100	192	143	135	-587	43	20	20	49
300	100	-10	-1	280	100	-43	140	132	-587	43	20	20	46

T [ns]	D [ns]	B [G]	m-state	f_{offset} [Hz]	P [%]	ν_{centre} [Hz]	$\delta\nu_{centre}$ [Hz]	$\delta\nu_{stat}$ [Hz]	$\Delta\nu_{slope}$ [Hz]	$\Delta\nu_{slope}$ [Hz]	$\Delta\nu_{zeem}$ [kHz]	$\delta\nu_{zeem}$	T_{total} [Mins]
300	100	-10	1	-280	100	59	156	149	-587	43	20	20	46
300	100	-10	1	280	100	195	152	145	-587	43	20	20	48
300	100	-5	-1	-280	20	9	138	137	-117	9	5	5	174
300	100	-5	-1	280	20	161	131	131	-117	9	5	5	180
300	100	-5	1	-280	20	191	143	143	-117	9	5	5	185
300	100	-5	1	280	20	-1	143	143	-117	9	5	5	184
300	100	-5	-1	-280	40	58	123	121	-235	17	5	5	96
300	100	-5	-1	280	40	-87	140	139	-235	17	5	5	98
300	100	-5	1	-280	40	-327	145	144	-235	17	5	5	104
300	100	-5	1	280	40	-173	146	145	-235	17	5	5	99
300	100	-5	-1	-280	60	42	120	118	-352	26	5	5	89
300	100	-5	-1	280	60	92	114	111	-352	26	5	5	92
300	100	-5	1	-280	60	-149	127	125	-352	26	5	5	97
300	100	-5	1	280	60	-24	134	131	-352	26	5	5	92
300	100	-5	-1	-280	80	-149	148	144	-470	34	5	5	46
300	100	-5	-1	280	80	-119	148	144	-470	34	5	5	46
300	100	-5	1	-280	80	246	149	145	-470	34	5	5	50
300	100	-5	1	280	80	271	145	141	-470	34	5	5	50
300	100	-5	-1	-280	100	215	134	127	-587	43	5	5	46
300	100	-5	-1	280	100	-5	142	135	-587	43	5	5	46
300	100	-5	1	-280	100	31	134	127	-587	43	5	5	50
300	100	-5	1	280	100	156	152	146	-587	43	5	5	52
300	100	5	-1	-280	20	70	146	146	-117	9	5	5	170
300	100	5	-1	280	20	-421	146	146	-117	9	5	5	170
300	100	5	1	-280	20	-21	134	133	-117	9	5	5	195
300	100	5	1	280	20	-201	140	140	-117	9	5	5	195
300	100	5	-1	-280	40	131	139	138	-235	17	5	5	92
300	100	5	-1	280	40	157	141	140	-235	17	5	5	92
300	100	5	1	-280	40	26	138	137	-235	17	5	5	99
300	100	5	1	280	40	185	132	131	-235	17	5	5	106
300	100	5	-1	-280	60	59	125	123	-352	26	5	5	85
300	100	5	-1	280	60	-46	126	123	-352	26	5	5	85

T [ns]	D [ns]	B [G]	m-state	f_{offset} [Hz]	P [%]	ν_{centre} [Hz]	$\delta\nu_{centre}$ [Hz]	$\delta\nu_{stat}$ [Hz]	$\Delta\nu_{slope}$ [Hz]	$\Delta\nu_{slope}$ [Hz]	$\Delta\nu_{zeem}$ [kHz]	$\delta\nu_{zeem}$	T_{total} [Mins]
300	100	5	1	-280	60	-109	120	117	-352	26	5	5	92
300	100	5	1	280	60	-165	113	110	-352	26	5	5	96
300	100	5	-1	-280	80	-99	157	153	-470	34	5	5	46
300	100	5	-1	280	80	-111	146	142	-470	34	5	5	46
300	100	5	1	-280	80	-98	138	134	-470	34	5	5	53
300	100	5	1	280	80	83	138	133	-470	34	5	5	53
300	100	5	-1	-280	100	197	136	129	-587	43	5	5	46
300	100	5	-1	280	100	-79	145	138	-587	43	5	5	46
300	100	5	1	-280	100	9	139	132	-587	43	5	5	50
300	100	5	1	280	100	89	129	122	-587	43	5	5	50
300	100	10	-1	-280	20	-157	153	152	-117	9	20	20	156
300	100	10	-1	280	20	-116	148	147	-117	9	20	20	156
300	100	10	1	-280	20	372	158	157	-117	9	20	20	184
300	100	10	1	280	20	152	156	154	-117	9	20	20	177
300	100	10	-1	-280	40	-108	142	139	-235	17	20	20	85
300	100	10	-1	280	40	142	150	148	-235	17	20	20	85
300	100	10	1	-280	40	115	159	156	-235	17	20	20	92
300	100	10	1	280	40	8	156	154	-235	17	20	20	99
300	100	10	-1	-280	60	-57	128	124	-352	26	20	20	78
300	100	10	-1	280	60	-199	128	123	-352	26	20	20	78
300	100	10	1	-280	60	130	132	128	-352	26	20	20	92
300	100	10	1	280	60	-38	142	138	-352	26	20	20	85
300	100	10	-1	-280	80	57	157	152	-470	34	20	20	43
300	100	10	-1	280	80	-121	157	152	-470	34	20	20	43
300	100	10	1	-280	80	-71	154	149	-470	34	20	20	50
300	100	10	1	280	80	-247	175	171	-470	34	20	20	46
300	100	10	-1	-280	100	-326	150	143	-587	43	20	20	42
300	100	10	-1	280	100	168	157	149	-587	43	20	20	43
300	100	10	1	-280	100	-5	146	138	-587	43	20	20	53
300	100	10	1	280	100	161	144	136	-587	43	20	20	53
300	100	15	-1	-280	20	158	175	169	-117	9	45	45	127
300	100	15	-1	280	20	-45	175	169	-117	9	45	45	127

T [ns]	D [ns]	B [G]	m-state	f_{offset} [Hz]	P [%]	ν_{centre} [Hz]	$\delta\nu_{centre}$ [Hz]	$\delta\nu_{stat}$ [Hz]	$\Delta\nu_{slope}$ [Hz]	$\Delta\nu_{slope}$ [Hz]	$\Delta\nu_{zeem}$ [kHz]	$\delta\nu_{zeem}$	T_{total} [Mins]
300	100	15	1	-280	20	-33	230	225	-117	9	45	45	130
300	100	15	1	280	20	-19	245	240	-117	9	45	45	120
300	100	15	-1	-280	40	55	183	176	-235	17	45	45	71
300	100	15	-1	280	40	155	176	169	-235	17	45	45	73
300	100	15	1	-280	40	67	229	224	-235	17	45	45	67
300	100	15	1	280	40	43	243	238	-235	17	45	45	67
300	100	15	-1	-280	60	-48	161	153	-352	26	45	45	64
300	100	15	-1	280	60	-101	152	142	-352	26	45	45	64
300	100	15	1	-280	60	-255	202	195	-352	26	45	45	60
300	100	15	1	280	60	-178	208	202	-352	26	45	45	60
300	100	15	-1	-280	80	164	171	162	-470	34	45	45	35
300	100	15	-1	280	80	205	184	175	-470	34	45	45	35
300	100	15	1	-280	80	-70	243	237	-470	34	45	45	35
300	100	15	1	280	80	571	223	216	-470	34	45	45	35
300	100	15	-1	-280	100	-176	172	161	-587	43	45	45	35
300	100	15	-1	280	100	-15	164	152	-587	43	45	45	35
300	100	15	1	-280	100	264	228	220	-587	43	45	45	32
300	100	15	1	280	100	35	240	232	-587	43	45	45	32
400	100	-15	-1	-280	20	366	295	292	-88	6	45	45	214
400	100	-15	-1	280	20	104	261	257	-88	6	45	45	247
400	100	-15	1	-280	20	389	293	289	-88	6	45	45	975
400	100	-15	1	280	20	-256	252	248	-88	6	45	45	998
400	100	-15	-1	-280	40	-46	274	270	-176	13	45	45	94
400	100	-15	-1	280	40	-20	262	258	-176	13	45	45	89
400	100	-15	1	-280	40	-285	335	331	-176	13	45	45	146
400	100	-15	1	280	40	60	331	327	-176	13	45	45	158
400	100	-15	-1	-280	60	-218	266	262	-264	19	45	45	55
400	100	-15	-1	280	60	228	238	233	-264	19	45	45	56
400	100	-15	1	-280	60	178	337	333	-264	19	45	45	67
400	100	-15	1	280	60	474	312	308	-264	19	45	45	69
400	100	-15	-1	-280	80	309	250	245	-352	26	45	45	42
400	100	-15	-1	280	80	182	275	270	-352	26	45	45	36

T [ns]	D [ns]	B [G]	m-state	f_{offset} [Hz]	P [%]	ν_{centre} [Hz]	$\delta\nu_{centre}$ [Hz]	$\delta\nu_{stat}$ [Hz]	$\Delta\nu_{slope}$ [Hz]	$\Delta\nu_{slope}$ [Hz]	$\Delta\nu_{zeem}$ [kHz]	$\delta\nu_{zeem}$	T_{total} [Mins]
400	100	-15	1	-280	80	522	327	323	-352	26	45	45	36
400	100	-15	1	280	80	-21	315	310	-352	26	45	45	45
400	100	-15	-1	-280	100	175	294	288	-440	32	45	45	32
400	100	-15	-1	280	100	494	238	231	-440	32	45	45	32
400	100	-15	1	-280	100	319	338	333	-440	32	45	45	32
400	100	-15	1	280	100	917	354	350	-440	32	45	45	32
400	100	-10	-1	-280	20	627	246	245	-88	6	20	20	306
400	100	-10	-1	280	20	137	227	226	-88	6	20	20	289
400	100	-10	1	-280	20	362	267	266	-88	6	20	20	752
400	100	-10	1	280	20	-273	274	274	-88	6	20	20	793
400	100	-10	-1	-280	40	-175	245	244	-176	13	20	20	93
400	100	-10	-1	280	40	262	232	231	-176	13	20	20	104
400	100	-10	1	-280	40	55	282	281	-176	13	20	20	156
400	100	-10	1	280	40	47	294	293	-176	13	20	20	146
400	100	-10	-1	-280	60	-319	235	234	-264	19	20	20	56
400	100	-10	-1	280	60	-247	208	206	-264	19	20	20	67
400	100	-10	1	-280	60	430	312	311	-264	19	20	20	54
400	100	-10	1	280	60	-253	271	270	-264	19	20	20	68
400	100	-10	-1	-280	80	277	253	251	-352	26	20	20	42
400	100	-10	-1	280	80	293	225	222	-352	26	20	20	41
400	100	-10	1	-280	80	340	321	319	-352	26	20	20	33
400	100	-10	1	280	80	154	344	343	-352	26	20	20	32
400	100	-10	-1	-280	100	-178	292	290	-440	32	20	20	28
400	100	-10	-1	280	100	-163	249	246	-440	32	20	20	28
400	100	-10	1	-280	100	-556	346	344	-440	32	20	20	30
400	100	-10	1	280	100	-77	337	335	-440	32	20	20	30
400	100	-5	-1	-280	20	362	269	269	-88	6	5	5	260
400	100	-5	-1	280	20	-163	254	254	-88	6	5	5	283
400	100	-5	1	-280	20	-105	219	218	-88	6	5	5	1026
400	100	-5	1	280	20	143	218	218	-88	6	5	5	870
400	100	-5	-1	-280	40	337	245	245	-176	13	5	5	83
400	100	-5	-1	280	40	-359	242	241	-176	13	5	5	93

T [ns]	D [ns]	B [G]	m-state	f_{offset} [Hz]	P [%]	ν_{centre} [Hz]	$\delta\nu_{centre}$ [Hz]	$\delta\nu_{stat}$ [Hz]	$\Delta\nu_{slope}$ [Hz]	$\Delta\nu_{slope}$ [Hz]	$\Delta\nu_{zeem}$ [kHz]	$\delta\nu_{zeem}$	T_{total} [Mins]
400	100	-5	1	-280	40	458	282	282	-176	13	5	5	148
400	100	-5	1	280	40	-168	265	265	-176	13	5	5	167
400	100	-5	-1	-280	60	-104	205	204	-264	19	5	5	64
400	100	-5	-1	280	60	204	215	214	-264	19	5	5	63
400	100	-5	1	-280	60	133	297	296	-264	19	5	5	63
400	100	-5	1	280	60	257	306	305	-264	19	5	5	51
400	100	-5	-1	-280	80	-23	226	224	-352	26	5	5	39
400	100	-5	-1	280	80	-274	236	235	-352	26	5	5	45
400	100	-5	1	-280	80	1256	316	315	-352	26	5	5	32
400	100	-5	1	280	80	176	330	329	-352	26	5	5	33
400	100	-5	-1	-280	100	49	211	208	-440	32	5	5	32
400	100	-5	-1	280	100	-224	226	224	-440	32	5	5	30
400	100	-5	1	-280	100	107	296	294	-440	32	5	5	30
400	100	-5	1	280	100	319	294	292	-440	32	5	5	30
400	100	5	-1	-280	20	-125	225	225	-88	6	5	5	882
400	100	5	-1	280	20	423	196	196	-88	6	5	5	839
400	100	5	1	-280	20	-93	259	259	-88	6	5	5	223
400	100	5	1	280	20	-167	264	264	-88	6	5	5	237
400	100	5	-1	-280	40	105	275	275	-176	13	5	5	155
400	100	5	-1	280	40	32	248	247	-176	13	5	5	164
400	100	5	1	-280	40	-102	244	243	-176	13	5	5	96
400	100	5	1	280	40	-570	227	227	-176	13	5	5	103
400	100	5	-1	-280	60	-242	278	278	-264	19	5	5	69
400	100	5	-1	280	60	-249	279	278	-264	19	5	5	64
400	100	5	1	-280	60	304	212	211	-264	19	5	5	65
400	100	5	1	280	60	291	242	241	-264	19	5	5	57
400	100	5	-1	-280	80	-387	275	274	-352	26	5	5	34
400	100	5	-1	280	80	71	325	324	-352	26	5	5	33
400	100	5	1	-280	80	312	216	214	-352	26	5	5	43
400	100	5	1	280	80	11	241	239	-352	26	5	5	42
400	100	5	-1	-280	100	297	296	294	-440	32	5	5	27
400	100	5	-1	280	100	205	300	298	-440	32	5	5	34

T [ns]	D [ns]	B [G]	m-state	f_{offset} [Hz]	P [%]	ν_{centre} [Hz]	$\delta\nu_{centre}$ [Hz]	$\delta\nu_{stat}$ [Hz]	$\Delta\nu_{slope}$ [Hz]	$\Delta\nu_{slope}$ [Hz]	$\Delta\nu_{zeem}$ [kHz]	$\delta\nu_{zeem}$	T_{total} [Mins]
400	100	5	1	-280	100	-122	223	220	-440	32	5	5	32
400	100	5	1	280	100	417	220	217	-440	32	5	5	32
400	100	10	-1	-280	20	26	229	228	-88	6	20	20	851
400	100	10	-1	280	20	373	249	248	-88	6	20	20	832
400	100	10	1	-280	20	610	285	285	-88	6	20	20	261
400	100	10	1	280	20	35	267	266	-88	6	20	20	231
400	100	10	-1	-280	40	-369	284	283	-176	13	20	20	125
400	100	10	-1	280	40	-29	288	287	-176	13	20	20	129
400	100	10	1	-280	40	-77	289	288	-176	13	20	20	83
400	100	10	1	280	40	-15	261	260	-176	13	20	20	99
400	100	10	-1	-280	60	124	312	310	-264	19	20	20	66
400	100	10	-1	280	60	38	297	296	-264	19	20	20	57
400	100	10	1	-280	60	-93	238	236	-264	19	20	20	62
400	100	10	1	280	60	-154	226	224	-264	19	20	20	67
400	100	10	-1	-280	80	390	326	325	-352	26	20	20	32
400	100	10	-1	280	80	-92	291	289	-352	26	20	20	39
400	100	10	1	-280	80	322	280	278	-352	26	20	20	43
400	100	10	1	280	80	574	261	259	-352	26	20	20	41
400	100	10	-1	-280	100	12	305	303	-440	32	20	20	30
400	100	10	-1	280	100	-50	275	273	-440	32	20	20	33
400	100	10	1	-280	100	185	266	264	-440	32	20	20	28
400	100	10	1	280	100	231	285	283	-440	32	20	20	28
400	100	15	-1	-280	20	-45	304	301	-88	6	45	45	1040
400	100	15	-1	280	20	-27	291	288	-88	6	45	45	1293
400	100	15	1	-280	20	82	247	243	-88	6	45	45	288
400	100	15	1	280	20	110	230	225	-88	6	45	45	306
400	100	15	-1	-280	40	-190	302	299	-176	13	45	45	214
400	100	15	-1	280	40	-154	298	294	-176	13	45	45	215
400	100	15	1	-280	40	-108	207	201	-176	13	45	45	134
400	100	15	1	280	40	115	219	214	-176	13	45	45	125
400	100	15	-1	-280	60	472	298	294	-264	19	45	45	96
400	100	15	-1	280	60	-460	316	312	-264	19	45	45	84

T [ns]	D [ns]	B [G]	m-state	f_{offset} [Hz]	P [%]	ν_{centre} [Hz]	$\delta\nu_{centre}$ [Hz]	$\delta\nu_{stat}$ [Hz]	$\Delta\nu_{slope}$ [Hz]	$\Delta\nu_{slope}$ [Hz]	$\Delta\nu_{zeem}$ [kHz]	$\delta\nu_{zeem}$	T_{total} [Mins]
400	100	15	1	-280	60	-60	202	197	-264	19	45	45	95
400	100	15	1	280	60	204	190	183	-264	19	45	45	88
400	100	15	-1	-280	80	494	323	319	-352	26	45	45	47
400	100	15	-1	280	80	527	318	314	-352	26	45	45	43
400	100	15	1	-280	80	-414	203	196	-352	26	45	45	60
400	100	15	1	280	80	-15	214	207	-352	26	45	45	59
400	100	15	-1	-280	100	-194	331	326	-440	32	45	45	43
400	100	15	-1	280	100	340	286	281	-440	32	45	45	43
400	100	15	1	-280	100	200	206	199	-440	32	45	45	53
400	100	15	1	280	100	185	201	194	-440	32	45	45	50
500	100	-5	-1	-280	20	-636	392	392	-70	5	5	5	113
500	100	-5	-1	280	20	326	324	324	-70	5	5	5	141
500	100	-5	1	-280	20	349	419	419	-70	5	5	5	141
500	100	-5	1	280	20	-137	375	375	-70	5	5	5	145
500	100	-5	-1	-280	40	129	394	394	-141	10	5	5	69
500	100	-5	-1	280	40	-211	306	306	-141	10	5	5	86
500	100	-5	1	-280	40	178	349	349	-141	10	5	5	86
500	100	-5	1	280	40	725	354	354	-141	10	5	5	86
500	100	-5	-1	-280	60	304	362	362	-211	15	5	5	59
500	100	-5	-1	280	60	131	248	247	-211	15	5	5	59
500	100	-5	1	-280	60	-68	305	304	-211	15	5	5	61
500	100	-5	1	280	60	-40	326	326	-211	15	5	5	59
500	100	-5	-1	-280	80	-33	259	258	-282	20	5	5	59
500	100	-5	-1	280	80	223	258	258	-282	20	5	5	61
500	100	-5	1	-280	80	310	291	291	-282	20	5	5	59
500	100	-5	1	280	80	438	304	304	-282	20	5	5	60
500	100	-5	-1	-280	100	50	352	351	-352	26	5	5	25
500	100	-5	-1	280	100	-257	348	347	-352	26	5	5	31
500	100	-5	1	-280	100	-141	366	365	-352	26	5	5	31
500	100	-5	1	280	100	544	362	361	-352	26	5	5	31
500	100	5	-1	-280	20	38	310	310	-70	5	5	5	141
500	100	5	-1	280	20	-364	331	331	-70	5	5	5	141

T [ns]	D [ns]	B [G]	m-state	f_{offset} [Hz]	P [%]	ν_{centre} [Hz]	$\delta\nu_{centre}$ [Hz]	$\delta\nu_{stat}$ [Hz]	$\Delta\nu_{slope}$ [Hz]	$\Delta\nu_{slope}$ [Hz]	$\Delta\nu_{zeem}$ [kHz]	$\delta\nu_{zeem}$	T_{total} [Mins]
500	100	5	1	-280	20	-329	279	279	-70	5	5	5	141
500	100	5	1	280	20	-460	362	362	-70	5	5	5	113
500	100	5	-1	-280	40	17	253	253	-141	10	5	5	87
500	100	5	-1	280	40	351	282	281	-141	10	5	5	86
500	100	5	1	-280	40	473	241	240	-141	10	5	5	69
500	100	5	1	280	40	308	342	342	-141	10	5	5	86
500	100	5	-1	-280	60	485	278	277	-211	15	5	5	59
500	100	5	-1	280	60	467	268	268	-211	15	5	5	59
500	100	5	1	-280	60	-303	293	293	-211	15	5	5	59
500	100	5	1	280	60	-154	322	322	-211	15	5	5	47
500	100	5	-1	-280	80	215	226	225	-282	20	5	5	59
500	100	5	-1	280	80	-10	250	249	-282	20	5	5	59
500	100	5	1	-280	80	-236	248	247	-282	20	5	5	59
500	100	5	1	280	80	-187	262	262	-282	20	5	5	59
500	100	5	-1	-280	100	108	283	281	-352	26	5	5	31
500	100	5	-1	280	100	-121	288	287	-352	26	5	5	36
500	100	5	1	-280	100	248	365	364	-352	26	5	5	31
500	100	5	1	280	100	-134	292	291	-352	26	5	5	31
400	200	-15	-1	-280	20	-136	214	209	-107	10	45	45	140
400	200	-15	-1	280	20	123	217	213	-107	10	45	45	139
400	200	-15	1	-280	20	76	176	170	-107	10	45	45	1221
400	200	-15	1	280	20	-352	160	153	-107	10	45	45	1326
400	200	-15	-1	-280	40	-208	241	236	-213	19	45	45	73
400	200	-15	-1	280	40	-60	231	226	-213	19	45	45	66
400	200	-15	1	-280	40	-415	188	182	-213	19	45	45	190
400	200	-15	1	280	40	70	196	190	-213	19	45	45	166
400	200	-15	-1	-280	60	-21	201	194	-320	29	45	45	48
400	200	-15	-1	280	60	-300	205	197	-320	29	45	45	60
400	200	-15	1	-280	60	100	188	180	-320	29	45	45	86
400	200	-15	1	280	60	25	176	168	-320	29	45	45	94
400	200	-15	-1	-280	80	-116	246	239	-426	39	45	45	35
400	200	-15	-1	280	80	289	206	197	-426	39	45	45	31

T [ns]	D [ns]	B [G]	m-state	f_{offset} [Hz]	P [%]	ν_{centre} [Hz]	$\delta\nu_{centre}$ [Hz]	$\delta\nu_{stat}$ [Hz]	$\Delta\nu_{slope}$ [Hz]	$\Delta\nu_{slope}$ [Hz]	$\Delta\nu_{zeem}$ [kHz]	$\delta\nu_{zeem}$	T_{total} [Mins]
400	200	-15	1	-280	80	-184	235	228	-426	39	45	45	39
400	200	-15	1	280	80	52	225	217	-426	39	45	45	38
400	200	-15	-1	-280	100	139	241	232	-533	49	45	45	39
400	200	-15	-1	280	100	-645	212	202	-533	49	45	45	25
400	200	-15	1	-280	100	69	207	197	-533	49	45	45	55
400	200	-15	1	280	100	58	205	194	-533	49	45	45	49
400	200	-10	-1	-280	20	-359	195	194	-107	10	20	20	153
400	200	-10	-1	280	20	196	202	200	-107	10	20	20	149
400	200	-10	1	-280	20	-69	132	130	-107	10	20	20	1397
400	200	-10	1	280	20	-42	140	138	-107	10	20	20	1181
400	200	-10	-1	-280	40	50	208	206	-213	19	20	20	78
400	200	-10	-1	280	40	73	199	197	-213	19	20	20	65
400	200	-10	1	-280	40	-69	165	162	-213	19	20	20	183
400	200	-10	1	280	40	202	156	153	-213	19	20	20	169
400	200	-10	-1	-280	60	-255	199	196	-320	29	20	20	51
400	200	-10	-1	280	60	-308	194	191	-320	29	20	20	49
400	200	-10	1	-280	60	219	153	149	-320	29	20	20	79
400	200	-10	1	280	60	-220	157	153	-320	29	20	20	82
400	200	-10	-1	-280	80	-238	231	226	-426	39	20	20	30
400	200	-10	-1	280	80	-200	220	215	-426	39	20	20	31
400	200	-10	1	-280	80	185	211	207	-426	39	20	20	35
400	200	-10	1	280	80	296	196	191	-426	39	20	20	38
400	200	-10	-1	-280	100	-57	209	202	-533	49	20	20	25
400	200	-10	-1	280	100	29	224	218	-533	49	20	20	25
400	200	-10	1	-280	100	-275	186	179	-533	49	20	20	50
400	200	-10	1	280	100	216	174	166	-533	49	20	20	54
400	200	-5	-1	-280	20	-223	186	186	-107	10	5	5	171
400	200	-5	-1	280	20	94	194	194	-107	10	5	5	192
400	200	-5	1	-280	20	-181	112	111	-107	10	5	5	1537
400	200	-5	1	280	20	54	118	118	-107	10	5	5	1353
400	200	-5	-1	-280	40	-29	200	199	-213	19	5	5	68
400	200	-5	-1	280	40	89	213	212	-213	19	5	5	81

T [ns]	D [ns]	B [G]	m-state	f_{offset} [Hz]	P [%]	ν_{centre} [Hz]	$\delta\nu_{centre}$ [Hz]	$\delta\nu_{stat}$ [Hz]	$\Delta\nu_{slope}$ [Hz]	$\delta\nu_{slope}$ [Hz]	$\Delta\nu_{zeem}$ [kHz]	$\delta\nu_{zeem}$	T_{total} [Mins]
400	200	-5	1	-280	40	-64	140	139	-213	19	5	5	189
400	200	-5	1	280	40	35	145	144	-213	19	5	5	170
400	200	-5	-1	-280	60	-84	184	181	-320	29	5	5	49
400	200	-5	-1	280	60	-189	173	171	-320	29	5	5	78
400	200	-5	1	-280	60	-35	135	132	-320	29	5	5	88
400	200	-5	1	280	60	-71	154	151	-320	29	5	5	85
400	200	-5	-1	-280	80	172	215	212	-426	39	5	5	32
400	200	-5	-1	280	80	-3	206	203	-426	39	5	5	64
400	200	-5	1	-280	80	259	200	196	-426	39	5	5	37
400	200	-5	1	280	80	149	187	183	-426	39	5	5	38
400	200	-5	-1	-280	100	-164	209	204	-533	49	5	5	39
400	200	-5	-1	280	100	255	199	193	-533	49	5	5	29
400	200	-5	1	-280	100	126	156	148	-533	49	5	5	50
400	200	-5	1	280	100	2	149	141	-533	49	5	5	49
400	200	5	-1	-280	20	-175	135	135	-107	10	5	5	906
400	200	5	-1	280	20	22	129	129	-107	10	5	5	1209
400	200	5	1	-280	20	-10	187	186	-107	10	5	5	211
400	200	5	1	280	20	63	179	179	-107	10	5	5	233
400	200	5	-1	-280	40	-131	146	144	-213	19	5	5	172
400	200	5	-1	280	40	151	146	144	-213	19	5	5	181
400	200	5	1	-280	40	-93	193	192	-213	19	5	5	65
400	200	5	1	280	40	188	196	195	-213	19	5	5	73
400	200	5	-1	-280	60	-157	128	124	-320	29	5	5	93
400	200	5	-1	280	60	-246	133	130	-320	29	5	5	86
400	200	5	1	-280	60	-173	167	164	-320	29	5	5	49
400	200	5	1	280	60	58	181	179	-320	29	5	5	55
400	200	5	-1	-280	80	-185	182	178	-426	39	5	5	44
400	200	5	-1	280	80	307	201	197	-426	39	5	5	38
400	200	5	1	-280	80	-60	210	207	-426	39	5	5	32
400	200	5	1	280	80	-69	207	204	-426	39	5	5	31
400	200	5	-1	-280	100	66	154	146	-533	49	5	5	49
400	200	5	-1	280	100	-287	167	160	-533	49	5	5	47

T [ns]	D [ns]	B [G]	m-state	f_{offset} [Hz]	P [%]	ν_{centre} [Hz]	$\delta\nu_{centre}$ [Hz]	$\delta\nu_{stat}$ [Hz]	$\Delta\nu_{slope}$ [Hz]	$\Delta\nu_{slope}$ [Hz]	$\Delta\nu_{zeem}$ [kHz]	$\delta\nu_{zeem}$	T_{total} [Mins]
400	200	5	1	-280	100	-396	199	193	-533	49	5	5	28
400	200	5	1	280	100	91	193	187	-533	49	5	5	28
400	200	10	-1	-280	20	-57	137	135	-107	10	20	20	1116
400	200	10	-1	280	20	85	132	130	-107	10	20	20	1124
400	200	10	1	-280	20	339	213	212	-107	10	20	20	199
400	200	10	1	280	20	122	204	203	-107	10	20	20	174
400	200	10	-1	-280	40	-55	152	149	-213	19	20	20	185
400	200	10	-1	280	40	4	144	142	-213	19	20	20	153
400	200	10	1	-280	40	52	230	228	-213	19	20	20	65
400	200	10	1	280	40	169	211	209	-213	19	20	20	71
400	200	10	-1	-280	60	-210	139	134	-320	29	20	20	93
400	200	10	-1	280	60	136	145	141	-320	29	20	20	87
400	200	10	1	-280	60	-20	191	188	-320	29	20	20	69
400	200	10	1	280	60	-173	192	189	-320	29	20	20	48
400	200	10	-1	-280	80	74	191	186	-426	39	20	20	38
400	200	10	-1	280	80	-49	214	209	-426	39	20	20	33
400	200	10	1	-280	80	-204	220	215	-426	39	20	20	32
400	200	10	1	280	80	99	256	252	-426	39	20	20	41
400	200	10	-1	-280	100	-232	154	144	-533	49	20	20	50
400	200	10	-1	280	100	-8	169	160	-533	49	20	20	48
400	200	10	1	-280	100	56	239	233	-533	49	20	20	25
400	200	10	1	280	100	-172	243	237	-533	49	20	20	25
400	200	15	-1	-280	20	17	161	155	-107	10	45	45	889
400	200	15	-1	280	20	3	152	145	-107	10	45	45	983
400	200	15	1	-280	20	184	252	248	-107	10	45	45	189
400	200	15	1	280	20	-60	251	247	-107	10	45	45	245
400	200	15	-1	-280	40	266	168	160	-213	19	45	45	154
400	200	15	-1	280	40	-463	164	156	-213	19	45	45	151
400	200	15	1	-280	40	-10	253	249	-213	19	45	45	82
400	200	15	1	280	40	-319	268	264	-213	19	45	45	67
400	200	15	-1	-280	60	-35	154	144	-320	29	45	45	82
400	200	15	-1	280	60	67	169	160	-320	29	45	45	77

T [ns]	D [ns]	B [G]	m-state	f_{offset} [Hz]	P [%]	ν_{centre} [Hz]	$\delta\nu_{centre}$ [Hz]	$\delta\nu_{stat}$ [Hz]	$\Delta\nu_{slope}$ [Hz]	$\Delta\nu_{slope}$ [Hz]	$\Delta\nu_{zeem}$ [kHz]	$\delta\nu_{zeem}$	T_{total} [Mins]
400	200	15	1	-280	60	-130	233	227	-320	29	45	45	49
400	200	15	1	280	60	454	225	219	-320	29	45	45	50
400	200	15	-1	-280	80	-367	245	238	-426	39	45	45	33
400	200	15	-1	280	80	-230	224	217	-426	39	45	45	32
400	200	15	1	-280	80	39	267	260	-426	39	45	45	37
400	200	15	1	280	80	80	300	294	-426	39	45	45	35
400	200	15	-1	-280	100	-173	162	148	-533	49	45	45	52
400	200	15	-1	280	100	196	174	161	-533	49	45	45	54
400	200	15	1	-280	100	261	261	253	-533	49	45	45	25
400	200	15	1	280	100	-106	277	269	-533	49	45	45	25
500	200	-15	-1	-280	20	-514	347	344	-85	8	45	45	169
500	200	-15	-1	280	20	171	372	370	-85	8	45	45	169
500	200	-15	1	-280	20	-327	344	341	-85	8	45	45	173
500	200	-15	1	280	20	-44	331	327	-85	8	45	45	169
500	200	-15	-1	-280	40	112	298	294	-171	16	45	45	103
500	200	-15	-1	280	40	-334	311	307	-171	16	45	45	103
500	200	-15	1	-280	40	-149	296	292	-171	16	45	45	103
500	200	-15	1	280	40	-22	279	275	-171	16	45	45	106
500	200	-15	-1	-280	60	-470	301	297	-256	23	45	45	71
500	200	-15	-1	280	60	-101	314	310	-256	23	45	45	71
500	200	-15	1	-280	60	429	215	209	-256	23	45	45	141
500	200	-15	1	280	60	-363	226	220	-256	23	45	45	106
500	200	-15	-1	-280	80	336	283	278	-341	31	45	45	71
500	200	-15	-1	280	80	-115	288	283	-341	31	45	45	71
500	200	-15	1	-280	80	-217	283	278	-341	31	45	45	71
500	200	-15	1	280	80	-85	294	289	-341	31	45	45	71
500	200	-15	-1	-280	100	32	355	351	-426	39	45	45	38
500	200	-15	-1	280	100	-241	348	343	-426	39	45	45	38
500	200	-15	1	-280	100	-573	362	357	-426	39	45	45	38
500	200	-15	1	280	100	-255	330	324	-426	39	45	45	38
500	200	-10	-1	-280	20	151	272	271	-85	8	20	20	169
500	200	-10	-1	280	20	-46	278	277	-85	8	20	20	169

T [ns]	D [ns]	B [G]	m-state	f_{offset} [Hz]	P [%]	ν_{centre} [Hz]	$\delta\nu_{centre}$ [Hz]	$\delta\nu_{stat}$ [Hz]	$\Delta\nu_{slope}$ [Hz]	$\Delta\nu_{slope}$ [Hz]	$\Delta\nu_{zeem}$ [kHz]	$\delta\nu_{zeem}$	T_{total} [Mins]
500	200	-10	1	-280	20	444	303	302	-85	8	20	20	169
500	200	-10	1	280	20	9	272	271	-85	8	20	20	169
500	200	-10	-1	-280	40	-330	276	275	-171	16	20	20	105
500	200	-10	-1	280	40	340	296	295	-171	16	20	20	103
500	200	-10	1	-280	40	54	279	277	-171	16	20	20	103
500	200	-10	1	280	40	56	217	215	-171	16	20	20	155
500	200	-10	-1	-280	60	-171	271	270	-256	23	20	20	71
500	200	-10	-1	280	60	293	255	253	-256	23	20	20	71
500	200	-10	1	-280	60	-217	236	234	-256	23	20	20	106
500	200	-10	1	280	60	-173	301	299	-256	23	20	20	71
500	200	-10	-1	-280	80	-199	251	248	-341	31	20	20	71
500	200	-10	-1	280	80	114	234	231	-341	31	20	20	71
500	200	-10	1	-280	80	-210	248	245	-341	31	20	20	71
500	200	-10	1	280	80	101	155	150	-341	31	20	20	141
500	200	-10	-1	-280	100	244	289	286	-426	39	20	20	38
500	200	-10	-1	280	100	-255	308	305	-426	39	20	20	38
500	200	-10	1	-280	100	-133	302	298	-426	39	20	20	38
500	200	-10	1	280	100	-215	280	277	-426	39	20	20	38
500	200	-5	-1	-280	20	72	281	281	-85	8	5	5	169
500	200	-5	-1	280	20	-406	287	287	-85	8	5	5	169
500	200	-5	1	-280	20	-236	262	262	-85	8	5	5	226
500	200	-5	1	280	20	279	229	229	-85	8	5	5	226
500	200	-5	-1	-280	40	-141	279	278	-171	16	5	5	103
500	200	-5	-1	280	40	299	275	275	-171	16	5	5	103
500	200	-5	1	-280	40	9	225	224	-171	16	5	5	138
500	200	-5	1	280	40	718	265	264	-171	16	5	5	86
500	200	-5	-1	-280	60	-552	279	278	-256	23	5	5	72
500	200	-5	-1	280	60	-18	277	276	-256	23	5	5	71
500	200	-5	1	-280	60	-146	266	265	-256	23	5	5	61
500	200	-5	1	280	60	408	299	298	-256	23	5	5	59
500	200	-5	-1	-280	80	-121	229	226	-341	31	5	5	71
500	200	-5	-1	280	80	-59	224	221	-341	31	5	5	71

T [ns]	D [ns]	B [G]	m-state	f_{offset} [Hz]	P [%]	ν_{centre} [Hz]	$\delta\nu_{centre}$ [Hz]	$\delta\nu_{stat}$ [Hz]	$\Delta\nu_{slope}$ [Hz]	$\Delta\nu_{slope}$ [Hz]	$\Delta\nu_{zeem}$ [kHz]	$\delta\nu_{zeem}$	T_{total} [Mins]
500	200	-5	1	-280	80	136	284	282	-341	31	5	5	59
500	200	-5	1	280	80	14	267	265	-341	31	5	5	59
500	200	-5	-1	-280	100	-549	326	323	-426	39	5	5	40
500	200	-5	-1	280	100	-120	296	293	-426	39	5	5	38
500	200	-5	1	-280	100	42	263	260	-426	39	5	5	52
500	200	-5	1	280	100	247	288	285	-426	39	5	5	31
500	200	5	-1	-280	20	-428	238	237	-85	8	5	5	226
500	200	5	-1	280	20	33	241	240	-85	8	5	5	226
500	200	5	1	-280	20	425	285	285	-85	8	5	5	171
500	200	5	1	280	20	-202	249	249	-85	8	5	5	169
500	200	5	-1	-280	40	-179	214	213	-171	16	5	5	141
500	200	5	-1	280	40	-329	266	265	-171	16	5	5	86
500	200	5	1	-280	40	-401	274	273	-171	16	5	5	103
500	200	5	1	280	40	-25	250	250	-171	16	5	5	105
500	200	5	-1	-280	60	-454	271	270	-256	23	5	5	59
500	200	5	-1	280	60	-318	258	257	-256	23	5	5	59
500	200	5	1	-280	60	-159	247	245	-256	23	5	5	71
500	200	5	1	280	60	-245	246	245	-256	23	5	5	71
500	200	5	-1	-280	80	-87	181	178	-341	31	5	5	94
500	200	5	-1	280	80	-273	237	235	-341	31	5	5	59
500	200	5	1	-280	80	-368	229	227	-341	31	5	5	71
500	200	5	1	280	80	19	222	220	-341	31	5	5	71
500	200	5	-1	-280	100	-393	333	331	-426	39	5	5	31
500	200	5	-1	280	100	-410	312	310	-426	39	5	5	31
500	200	5	1	-280	100	-926	286	283	-426	39	5	5	38
500	200	5	1	280	100	-119	261	258	-426	39	5	5	38
500	200	10	-1	-280	20	-332	296	296	-85	8	20	20	171
500	200	10	-1	280	20	-96	286	285	-85	8	20	20	169
500	200	10	1	-280	20	-558	250	249	-85	8	20	20	172
500	200	10	1	280	20	523	274	274	-85	8	20	20	169
500	200	10	-1	-280	40	-390	272	271	-171	16	20	20	105
500	200	10	-1	280	40	-303	217	216	-171	16	20	20	155

T [ns]	D [ns]	B [G]	m-state	f_{offset} [Hz]	P [%]	ν_{centre} [Hz]	$\delta\nu_{centre}$ [Hz]	$\delta\nu_{stat}$ [Hz]	$\Delta\nu_{slope}$ [Hz]	$\Delta\nu_{slope}$ [Hz]	$\Delta\nu_{zeem}$ [kHz]	$\delta\nu_{zeem}$	T_{total} [Mins]
500	200	10	1	-280	40	-364	252	250	-171	16	20	20	103
500	200	10	1	280	40	95	260	259	-171	16	20	20	103
500	200	10	-1	-280	60	52	256	254	-256	23	20	20	71
500	200	10	-1	280	60	-615	265	263	-256	23	20	20	71
500	200	10	1	-280	60	-177	265	263	-256	23	20	20	71
500	200	10	1	280	60	-113	267	265	-256	23	20	20	71
500	200	10	-1	-280	80	-369	216	213	-341	31	20	20	71
500	200	10	-1	280	80	-166	237	234	-341	31	20	20	71
500	200	10	1	-280	80	157	213	210	-341	31	20	20	71
500	200	10	1	280	80	169	238	235	-341	31	20	20	71
500	200	10	-1	-280	100	-108	235	231	-426	39	20	20	57
500	200	10	-1	280	100	-530	241	237	-426	39	20	20	57
500	200	10	1	-280	100	-494	302	299	-426	39	20	20	38
500	200	10	1	280	100	-84	304	301	-426	39	20	20	38
500	200	15	-1	-280	20	-738	303	300	-85	8	45	45	172
500	200	15	-1	280	20	-305	325	321	-85	8	45	45	172
500	200	15	1	-280	20	-483	326	323	-85	8	45	45	170
500	200	15	1	280	20	-115	348	345	-85	8	45	45	169
500	200	15	-1	-280	40	-798	316	312	-171	16	45	45	103
500	200	15	-1	280	40	-242	307	303	-171	16	45	45	103
500	200	15	1	-280	40	-792	300	296	-171	16	45	45	103
500	200	15	1	280	40	-274	343	339	-171	16	45	45	103
500	200	15	-1	-280	60	-330	301	297	-256	23	45	45	71
500	200	15	-1	280	60	91	301	296	-256	23	45	45	71
500	200	15	1	-280	60	-461	280	276	-256	23	45	45	73
500	200	15	1	280	60	-51	282	277	-256	23	45	45	75
500	200	15	-1	-280	80	-85	255	249	-341	31	45	45	71
500	200	15	-1	280	80	-43	205	198	-341	31	45	45	106
500	200	15	1	-280	80	-50	262	257	-341	31	45	45	73
500	200	15	1	280	80	-197	245	239	-341	31	45	45	71
500	200	15	-1	-280	100	-449	348	343	-426	39	45	45	38
500	200	15	-1	280	100	140	265	258	-426	39	45	45	57

T [ns]	D [ns]	B [G]	m-state	f_{offset} [Hz]	P [%]	ν_{centre} [Hz]	$\delta\nu_{centre}$ [Hz]	$\delta\nu_{stat}$ [Hz]	$\Delta\nu_{slope}$ [Hz]	$\Delta\nu_{slope}$ [Hz]	$\Delta\nu_{zeem}$ [kHz]	$\delta\nu_{zeem}$	T_{total} [Mins]
500	200	15	1	-280	100	80	329	324	-426	39	45	45	38
500	200	15	1	280	100	267	367	363	-426	39	45	45	38
600	200	-5	-1	-280	20	536	343	342	-71	6	5	5	555
600	200	-5	-1	280	20	-561	358	358	-71	6	5	5	558
600	200	-5	1	-280	20	302	404	404	-71	6	5	5	555
600	200	-5	1	280	20	152	397	397	-71	6	5	5	561
600	200	-5	-1	-280	40	-270	297	297	-142	13	5	5	338
600	200	-5	-1	280	40	-341	283	283	-142	13	5	5	339
600	200	-5	1	-280	40	321	327	327	-142	13	5	5	338
600	200	-5	1	280	40	327	336	336	-142	13	5	5	336
600	200	-5	-1	-280	60	104	280	280	-213	19	5	5	224
600	200	-5	-1	280	60	466	321	320	-213	19	5	5	201
600	200	-5	1	-280	60	-228	314	314	-213	19	5	5	227
600	200	-5	1	280	60	-507	296	295	-213	19	5	5	227
600	200	-5	-1	-280	80	199	243	241	-284	26	5	5	220
600	200	-5	-1	280	80	9	253	252	-284	26	5	5	220
600	200	-5	1	-280	80	154	232	231	-284	26	5	5	228
600	200	-5	1	280	80	104	249	248	-284	26	5	5	227
600	200	-5	-1	-280	100	-766	310	308	-355	32	5	5	117
600	200	-5	-1	280	100	504	331	330	-355	32	5	5	102
600	200	-5	1	-280	100	-281	326	324	-355	32	5	5	117
600	200	-5	1	280	100	432	309	307	-355	32	5	5	118
600	200	5	-1	-280	20	-16	348	348	-71	6	5	5	557
600	200	5	-1	280	20	315	346	346	-71	6	5	5	557
600	200	5	1	-280	20	-287	371	371	-71	6	5	5	560
600	200	5	1	280	20	349	343	343	-71	6	5	5	555
600	200	5	-1	-280	40	-401	269	269	-142	13	5	5	336
600	200	5	-1	280	40	405	280	280	-142	13	5	5	340
600	200	5	1	-280	40	-90	265	264	-142	13	5	5	339
600	200	5	1	280	40	-161	286	285	-142	13	5	5	339
600	200	5	-1	-280	60	-309	247	246	-213	19	5	5	227
600	200	5	-1	280	60	375	248	247	-213	19	5	5	227

T [ns]	D [ns]	B [G]	m-state	f_{offset} [Hz]	P [%]	ν_{centre} [Hz]	$\delta\nu_{centre}$ [Hz]	$\delta\nu_{stat}$ [Hz]	$\Delta\nu_{slope}$ [Hz]	$\Delta\nu_{slope}$ [Hz]	$\Delta\nu_{zeem}$ [kHz]	$\delta\nu_{zeem}$	T_{total} [Mins]
600	200	5	1	-280	60	-144	278	277	-213	19	5	5	200
600	200	5	1	280	60	242	292	291	-213	19	5	5	221
600	200	5	-1	-280	80	-605	213	211	-284	26	5	5	229
600	200	5	-1	280	80	-34	209	207	-284	26	5	5	227
600	200	5	1	-280	80	-153	247	245	-284	26	5	5	221
600	200	5	1	280	80	209	262	261	-284	26	5	5	222
600	200	5	-1	-280	100	-161	273	271	-355	32	5	5	117
600	200	5	-1	280	100	205	278	276	-355	32	5	5	117
600	200	5	1	-280	100	-236	313	311	-355	32	5	5	114
600	200	5	1	280	100	82	301	299	-355	32	5	5	116